University of Colorado, Boulder
CU Scholar

Undergraduate Honors Theses | Honors Program

Spring 2013

Trapping and Cooling Silica Microspheres

Alec Jenkins
University of Colorado Boulder

Follow this and additional works at: http://scholar.colorado.edu/honr_theses

Recommended Citation
Jenkins, Alec, "Trapping and Cooling Silica Microspheres" (2013). *Undergraduate Honors Theses.* Paper 387.

This Thesis is brought to you for free and open access by Honors Program at CU Scholar. It has been accepted for inclusion in Undergraduate Honors Theses by an authorized administrator of CU Scholar. For more information, please contact cuscholaradmin@colorado.edu.

Trapping and Cooling Silica Microspheres

by

Alec Jenkins

University of Colorado Department of Physics

2013

Advisor:

Professor Cindy Regal, Physics

Committee members:

Professor Jeanne Clelland, Mathematics

Professor Heather Lewandowski, Physics

This thesis entitled:
Trapping and Cooling Silica Microspheres
written by Alec Jenkins
has been approved for the Department of Physics

_____

Cindy Regal

_____

Heather Lewandowski

_____

Jeanne Clelland

Date _____

The final copy of this thesis has been examined by the signatories, and we find that both the content and the form meet acceptable presentation standards of scholarly work in the above mentioned discipline.

Jenkins, Alec (B.A., Physics)

Trapping and Cooling Silica Microspheres

Thesis directed by Professor Cindy Regal

Experiments in the field of cavity optomechanics have recently demonstrated the cooling of macroscopic mechanical systems to the quantum regime. In this paper, a system is presented which represents progress towards a particular realization of optical-mechanical coupling. In the proposed experiment, the center-of-mass motion of a levitated particle would be cooled to the ground state of an optical trap using the techniques of cavity optomechanics. Studying the quantum mechanics of macroscopic systems is of interest because the scales involved might allow for the study of phenomena related to both gravity and quantum mechanics. A system of this sort may also have applications in detection of extremely small forces or in quantum information experiments. This paper describes an apparatus which represents the first steps towards the ground state cooling of an optically levitated silica particle.

Acknowledgements

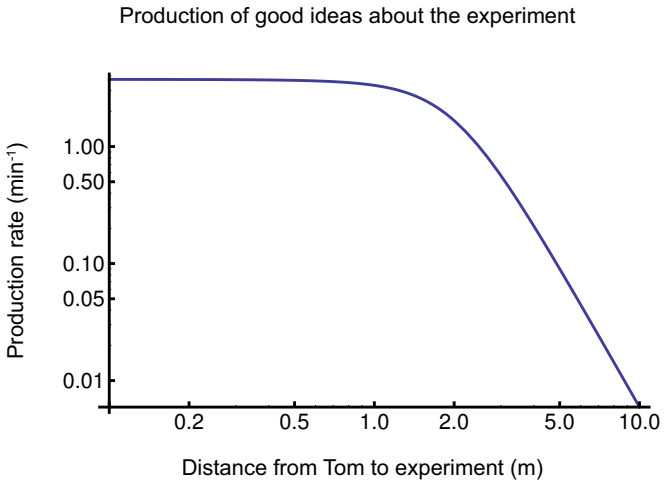

This experiment was the perfect culmination of my undergraduate career. It required an understanding of the concepts from almost every single course in physics I have taken. The experiment also served as a bridge from those concepts to the realities of experimental physics, and it did this in the harshest possible way. I am grateful that Cindy had the insight to give this project to an undergraduate. She has provided me with space and resources for this experiment, and she has encouraged me to step back and view the experiment as a whole.

I cannot accurately portray how helpful Tom has been. He has shown me how much fun experimental physics can be and I am constantly amazed by the depth of his knowledge in all areas of physics. Adam and Brian have been happy to answer any questions I have and do not complain when I regularly raid their optics drawer. Ben is always kind, and he helped me to feel comfortable in the lab when I first joined. I would like to thank Bob for his dark sense of humor. Everyone in the lab has been extremely nice and easy-going.

Contents

Chapter

1 Introduction 1

2 Background 3

2.1 The measurement problem 3

2.2 Decoherence 4

2.3 Gravitational State Reduction 5

2.4 Cavity optomechanics 6

2.5 Levitated nanospheres 7

3 Ion and optical traps 10

3.1 Ion traps 11

3.1.1 Ideal Paul traps 11

3.1.2 Gas damping in ion traps 14

3.2 Optical traps 17

3.2.1 Ray optics regime 18

3.2.2 Rayleigh regime 18

3.2.3 Scattering and perturbing forces 20

4 Equations of motion in a harmonic trap 22

4.1 Langevin equation 22

4.2 Feedback and measurement 23

5 Experimental apparatus 25

5.0.1 Paul trap and feedback electrodes 26

5.0.2 Optical trap 28

6 Results 30

6.1 Optical trap at atmospheric pressure 30

6.2 Ion trap cooling in vacuum 32

6.3 Optical trap cooling in vacuum 35

7 Conclusions 39

Bibliography 42

Appendix

A Density Matrices 44

B Decoherence 45

C Measurement calibration 47

D Measurement error and feedback 48

Figures

Figure

2.1 Side-band cooling in an optical cavity. 6

2.2 Experimental protocol for test of gravitationally-induced state reduction. 8

3.1 Hybrid ion-optical trap. 10

3.2 Ideal Paul trap. 12

3.3 First stability region for an ideal Paul trap. 13

3.4 Transition to unstable ion trap without damping. 15

3.5 Transition to unstable ion trap with damping. 15

3.6 Comparison of ion trap motion for particles of different sizes. 16

3.7 Ray optics for optical tweezers. 18

4.1 Power spectrum with active feedback. 24

5.1 One-beam optical trap with 780 nm imaging beam. 25

5.2 Paul trap schematic. 26

5.3 PD Circuit. 27

5.4 Two-beam optical trap. 29

6.1 Power spectrums for optical trap at atmospheric pressure. 31

6.2 Power spectrums for ion trap at mTorr pressure. 33

6.3 Power spectrums and derivative feedback phase. 34

6.4 Proportional feedback and damping factor. 35

6.5 Two-beam optical trap in vacuum. 36

6.6 Ideal pressure pressure dependence of power spectrum. 36

6.7 Two-beam optical trap in vacuum, temperature 37

6.8 Two-beam optical trap in vacuum set 2. 38

C.1 Signal calibration. 47

D.1 Feedback coupling. 49

Chapter 1

Introduction

Cavity optomechanics experiments harness and study the coupling between optical fields and mechanical systems inside optical resonators. Recently, it has been demonstrated that the interaction of a mechanical and optical field inside an optical cavity can be used to finely control the behavior of the mechanical system [1, 2, 3, 4]. These mechanical systems have represented a wide range of geometries and scales— from optically levitated particles with masses around 10^{-18} kg to suspended mirrors with masses around 40 kg [5, 6]. In some experiments, there has been success in observing quantum phenomena in macroscopic mechanical objects themselves, or in their optical measurement [7, 8, 9]. These experiments involve objects with larger masses than typical in quantum experiments, and this gives them the potential to explore certain theories describing the transition from quantum to classical behavior.

Since the formulation of quantum mechanics, the Copenhagen interpretation has been the orthodox view on how classical behavior emerges from quantum systems. However, in the 1980s, interest in quantum information and computation led to a reexamination of the border region between the classical and quantum worlds; new theories were created that attempted to explain the transition from quantum to classical behavior using only a system's interaction with its environment. This interaction results in a process known as decoherence because system-environment coupling causes the system's coherent superpositions to evolve into classical probability mixtures. [10]

Recent advances in the manipulation of small mechanical systems inside optical cavities have presented a new opportunity to experimentally test theories of the quantum-to-classical transition that go beyond the theory of environmentally induced decoherence [1, 4, 11, 12]. One idea, the

theory of gravitational state reduction, attempts to explain the quantum-to-classical transition using gravitational effects. Gravitational state collapse has been proposed through rough arguments involving the self-gravitational energy of a quantum superposition. These arguments do not stem from a complete theory of quantum gravity, so the scales involved are very speculative. As described by Penrose [13], these arguments give a "plausible" self-gravitational energy scale. The uncertainty involved in this scale makes an experimental probe of the large-mass quantum regime all the more intriguing.

A particular experiment involving optically levitated silica particles has been shown to be a candidate for testing the predictions of these theories [14, 15]. The mass and length scales of this experiment make it quite delicate; macroscopic systems ordinarily behave classically because they are strongly coupled to their environments. For this reason, probing the quantum regime of a macroscopic (or mesoscopic) system requires a very thorough decoupling of the system and environment. One method for obtaining a very isolated macroscopic system would be to levitate a particle in ultrahigh vacuum. While this system could possibly allow for the study of relationships between gravity and quantum mechanics, it could also find more functional applications in the detection of very small forces or in the study of quantum information [14].

This paper describes an apparatus which represents a preliminary step towards the ground-state cooling of a levitated particle. It begins with an introduction to the basic principles of side-band cooling in optical cavities. Then the levitated particle system is described in detail, and some of the experiment's components are examined. Finally, the results of active feedback cooling in our apparatus are given and compared those obtained in similar experiments [16, 17]. This work builds on that by C. Alvarez [18], who demonstrated the trapping of silica microspheres in an ion trap, and also built some components of the apparatus used in this work.

Chapter 2

Background

2.1 The measurement problem

The basic principles of quantum mechanics were discovered close to 100 years ago, and since that time, these principles have withstood every single experimental test of the theory [19]. Despite this, the basic predictions of quantum mechanics continue to puzzle. This is due to differences between what the equations of the theory imply and what we ordinarily perceive [10]. An important feature of quantum mechanics is its ability to describe a quantum mechanical system in terms of a superposition of states in a particular basis. Each of these states may have different physical properties and the system itself may have a superposition of physical properties. For example, the ground state of the hydrogen atom can be described as a superposition of electron-position states. So while it is reasonable to talk about the energy of the hydrogen ground state, it is not reasonable to talk about the position of the electron in this state. This feature of quantum systems is unlike anything we experience in the classical systems around us.

In order to explain the differences between quantum behavior and our classical expectations, the early developers of quantum mechanics appealed to a process called wavefunction collapse. As described by Zurek [10], the inclusion of wavefunction collapse in quantum mechanics gives the theory two different channels by which states can evolve— through unitary time evolution as described by the Schrodinger equation or through a non-unitary process by which measurement of an observable collapses the state to an eigenstate of that observable. Once the system is in an eigenstate of the observable, it has a well-defined value for that observable. While wavefunction collapse does explain how the superpositions of quantum mechanics are destroyed, Zurek points

out a fundamental flaw with this picture of quantum mechanics. The Copenhagen interpretation defines a measurement as the result of the interaction of a classical measuring device with a quantum system, but this definition does not explain what constitutes a classical device. Experiments involving macroscopic numbers of particles collectively behaving quantum mechanically seem to imply that the common notion of quantum as microscopic and classical as macroscopic is not valid [19].

The problems with the Copenhagen interpretation were acknowledged long before theories of decoherence were created. To avoid the measurement problems introduced by the Copenhagen interpretation, Everett [20] created another theory, the many-worlds interpretation. This theory attempted to do away with the boundary region between quantum and classical by describing the whole universe as a state vector. In this interpretation, interactions between quantum systems cause the universe to split into various branches, each of which represents a term in the superposition of the universes state. However, as Zurek explains, this theory does not quite accomplish its goal, for it fails to explain why observers experience only one of the universe's alternatives. Also, this theory does not explain which basis of the universal Hilbert space corresponds to the branches of the universe.

2.2 Decoherence

In order to solve the measurement problem, theories of decoherence appeal to a fact that has been known since the beginnings of quantum mechanics— macroscopic systems are strongly coupled to their environments [19]. This coupling can be used to explain how classical outcomes emerge from quantum mechanical systems. In order to see how this occurs, one has to examine the Hamiltonian of the joint system/environment [10]. The interaction term of this Hamiltonian causes the loss of information about the quantum system in such a way that certain superposition terms of the state decay over time [21]. Assuming an environment with a large number of degrees of freedom, this loss is an irreversible process, similar to that of heat flow (actually, it can be described in terms of entropy production) [10, 19]. As shown by Zurek [21], the specifics of the

system-environment interaction determine in what part of the quantum system the information is lost. For example, if a certain observable commutes with the interaction Hamiltonian, then the superposition information about this observable will be lost to the environment. After this loss has occurred, the system is left in a classical mixture of the eigenstates of the observable (that is, there is a classical probability of the state being in any one of the observable's eigenstates). To get a more rigorous picture of this process, it helps to introduce a mathematical tool called a density matrix. Appendix A contains information about density matrices and Appendix B describes decoherence in more mathematical terms.

2.3 Gravitational State Reduction

Environment-induced decoherence uses system-environment interaction to explain how classical mechanics can emerge from quantum mechanics, but there are other proposals for how this transition could occur. One of these proposals, put forward by Penrose [13], attempts to explain why quantum superpositions are not observed at macroscopic scales by using the laws of general relativity. According to Penrose's theory, superpositions decay on a time-scale T determined by the self-gravitational energy of the state E_Δ, $T \approx \hbar/E_\Delta$. Taking this point of view, it is possible that the entanglement of a quantum system with an environment causes the collapse of superpositions based on the gravitational-self energy of the system and environment as well as the irreversible nature of the system-environment interaction. In order to compare the theories of gravitationally induced state collapse and environmentally-induced decoherence, an experiment is needed in which a position-superposition can be created with a large enough gravitational self-energy and a small enough environmental decoherence rate such that the decay of the superposition due to gravity can be observed. This requires a mechanical system with a large mass and a weak coupling to its environment. As mentioned previously, the time and energy scales at which gravitational effects become important is not well known. The levitated particle experiment has the ability to either detect the gravitational effects or put constraints on these theories.

2.4 Cavity optomechanics

The field of cavity optomechanics is concerned with the coupling of optical and mechanical systems. The optical forces on nano-mechanical systems are inherently small (photons carry little momentum), but by placing a mechanical system inside an optical cavity, these forces can be exaggerated [1, 11]. Photons in an optical cavity can make many round trips between mirrors before leaving the cavity, so there is a greater probability of photon-mechanical system interaction. Through control of the light's intensity and frequency, optical-mechanical coupling can be used to manipulate the motion of a mechanical system. In many recent experiments, this coupling has been used to dampen the mechanical systems motion. The result is a net cooling of the mechanical vibrations in the system. This is accomplished by red-detuning the light slightly from a cavity resonance. Oscillations of the mechanical system will scatter light that is modulated by the mechanical frequency [1]. Figure 2.1 depicts the sidebands produced by this scattering. If the light is red-detuned from resonance by the mechanical frequency, then the light is preferentially scattered into the cavity resonance because the density of photon states is highest at resonance. The net effect of this scattering into a higher frequency is the transfer of energy from the mechanical object to the cavity's fields.

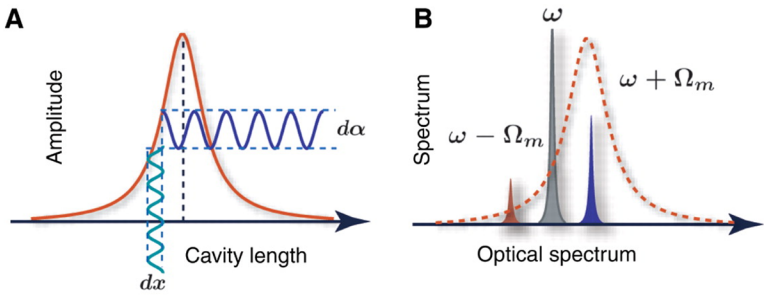

Figure 2.1: (a) Cavity length vs. intra-cavity field amplitude (b) Red-detuning and mechanically modulated sidebands. Diagram from [1].

This sideband-cooling technique has been successfully used to cool some nano and micromechanical systems to their ground states [7, 8]. In experiments such as these, the mechanical objects

are rigidly supported by a base. The thermal contact of these supports limits the amount of time for which the objects can remain at low occupation numbers without cooling. For this reason, these experiments are often carried out on systems that have been cooled cryogenically to a few Kelvin. A levitated nanosphere in vacuum can circumvent this problem by completely removing the mechanical systems support structure. Removing the support structure gives a system with much lower decoherence and thermalization rates, so it is possible that a levitated nanosphere would be sensitive to effects related to decoherence occurring on a longer time-scale [14]. It has been proposed that these effects could include phenomena related to both gravity and quantum mechanics [13, 15]. Lower decoherence and thermalization rates could be obtained in this system by dropping the particle from the trap (turning off the trap light).

The levitated silica particle is reminiscent of cold gas experiments, which also the study of the collective quantum mechanical properties of a larger number of atoms. However, using a silica particle has a few advantages in the exploration of the quantum-to-classical transition. The masses of levitated silica particles can be several orders of magnitude larger than a cooled gas. The smallest silica particles proposed for this experiment have radii around 50 nm. The mass of a silica particle this size is comparable to a Bose-Einstein Condensate (BEC) with 10^7 atoms, but BEC cavity optomechanics experiments, thus far, have consisted of smaller atom numbers (10^3 to 10^4) [22, 23]. While BEC experiments often have atom numbers around 10^7, the larger volume occupied by a BEC of this size leads to difficulties when implementing the side-band cooling techniques discussed above [22].

2.5 Levitated nanospheres

In a levitated nanosphere experiment, a dielectric sphere is trapped inside an optical cavity in laser light at the cavity's resonance frequency and a red-detuned beam of light is used to cool the bead's center of mass along the cooling beams axis. In one possible protocol, once the center of mass is cooled to the ground state of the optical trap, the trapping light is turned off, and a superposition of the beads momentum is prepared using a non-classical pulse of light. The wavefunction of the

bead is then allowed to expand for a set amount of time, and the superposition of momentum evolves into a superposition of location. At this point, an imaging beam is turned on and the position of the bead is measured. In order to observe the interference pattern expected based on the superposition, this procedure would need to be repeated enough times to resolve the pattern. The procedure is depicted in Fig. 2.2. By changing the amount of time that the wavefunction is allowed to expand, it should be possible to observe the decay of the superposition. The time scale of the decay of the superposition in this experiment could serve as either a confirmation or rejection of gravitationally induced state collapse [15].

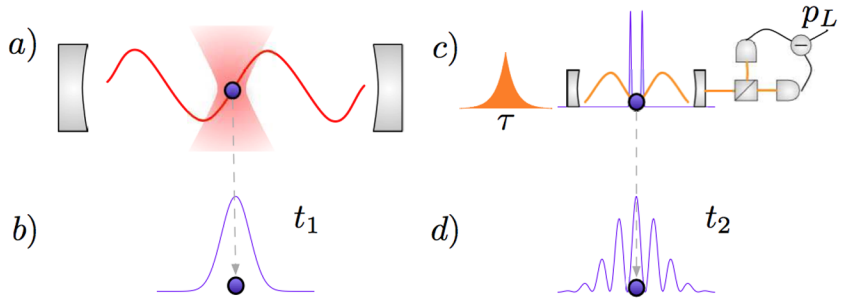

Figure 2.2: Experimental protocol for test of gravitationally-induced state reduction [15]. (a) Nanosphere cooled to ground state (b) Optical trap turned off (c) Superposition of momentum produced using non-classical pulse of light (d) Wavefunction of sphere expands and position is measured, revealing an interference pattern.

The time scale for the gravitational decay of superpositions is approximately $\hbar/E_\Delta$, where E_Δ is the uncertainty in the gravitational self-energy [13]. This term can be written in terms of physical parameters relevant to the levitated particle experiment. For some undetermined length scale of the superposition L, particle mass M, and universal gravitational constant G, the "plausible" time scale of gravitational state collapse can be written as $\tau \propto \hbar L/GM^2$ [24]. A study done by O. Romero-Isart et al. [15] shows that extremely high vacuum is required in order to preserve the coherent quantum states described in Fig. 2.2 for significant amounts of time. Operating in ultrahigh vacuum slows the ordinarily dominant decoherence rate that results from interactions

between the system and background gas. This study also found that the required amount of time to drop the nanoparticle is also determined by the position resolution of detectors in the experiment. So the state of the sphere needs to expand for a duration long enough that the fringes of the interference pattern are larger than the detection resolution.

Chapter 3

Ion and optical traps

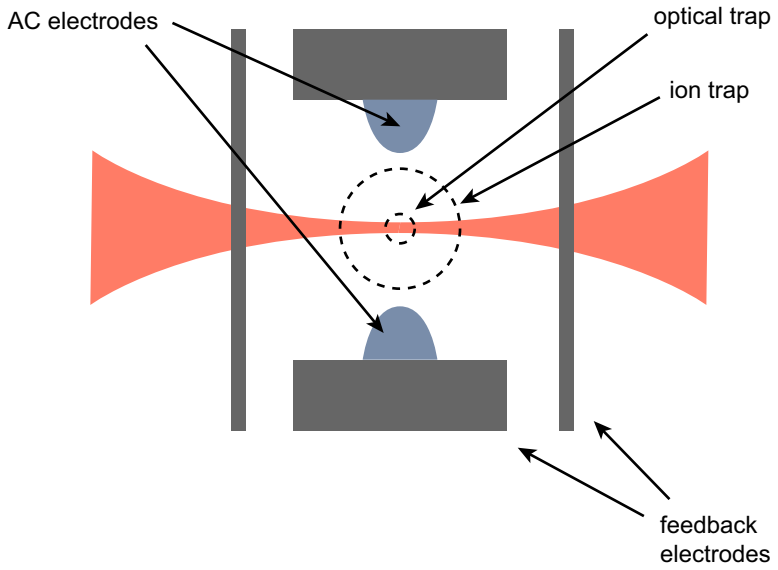

Figure 3.1: Hybrid ion-optical trap. The stable trapping region of the ion trap is much larger than that of optical trap, so the ion trap can be used as a loading mechanism for the optical trap.

Observation of interference fringes in the experiment described above (Sec. 2.5) requires that the preparation and observation of a particular state is repeatable. That is, in order to observe the interference pattern, many position measurements are required. To make the experiment repeatable, there must be a way to reload the optical trap after a position measurement has taken place. If there is any systematic drift in the particle's position during one cycle of the experiment, or if cooling and observation intentionally occur in different locations, then an ion trap could be useful in the process of reloading the optical trap. While an optical trap is limited in its scale, on the order of microns in the radially direction, an ion trap can occupy a much larger volume as long as

a high enough voltage is applied to the electrodes. For this reason our experimental apparatus has been designed with a hybrid ion-optical trap (Fig. 3.1).

3.1 Ion traps

Understanding the behavior of a particle in an ion trap is important to this experiment. The equation of motion in the trap specifies the timescales necessary for repetition of the experiment and influences the design of the hybrid trap. We have found that the effects of gas damping in the trap determine which sizes of particles can be stably trapped. At this stage, operation of the trap is also important in the characterization of particle behavior at low pressure.

Any three-dimensional trap requires a potential energy minimum at the trapping location. A general, three-dimensional trap has a potential $\phi = (\phi_0/d^2)(Ax^2 + By^2 + Cz^2)$ with A, B, and C positive. Examining Laplace's equation $\nabla^2\phi = 0$, one can see that this form of potential cannot be produced using static electric fields. The relation $A + B + C = 0$ implies that the potential due to static fields will have a saddle shape. In order to create an electric trap, which is stable in all three dimensions, ion traps use a time-varying, inhomogeneous electric field. The inhomogeneity of the field means that, over many oscillation cycles of the field, there exists a non-zero average force on a charged particle. Depending on the frequency of the trap and amplitude of the oscillating field, this average force can point towards or away from the center of the trap. [25]

3.1.1 Ideal Paul traps

Many different geometries of electrodes are used in ion traps. Our particular trap is most easily modeled by an ideal Paul trap (Fig. 3.2). See Fig. 5.2 for more information on our exact trap geometry. The ideal Paul trap consists of two hyberbolic (endcap) electrodes and a revolved hyperbolic sheet (ring) electrode, and is similar to the one used in our experiment. If an oscillating electric potential (angular frequency Ω) is applied to the endcap electrodes, while keeping the ring

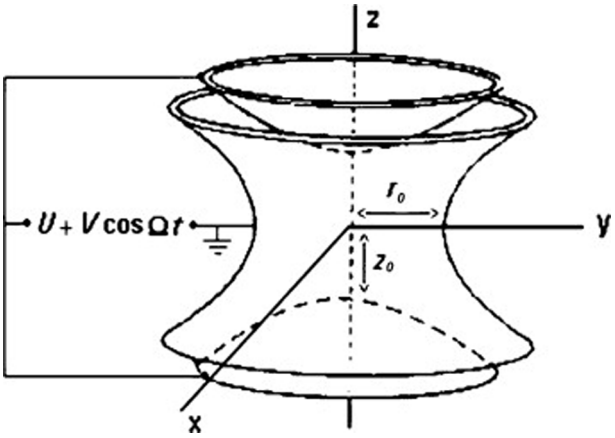

Figure 3.2: Ideal Paul trap. The electrodes are all hyperbolic surfaces sharing an asymptotic cone. Image from [26].

electrode grounded, the potential will be given by [25]

$$\phi = \frac{U_0 + V_0 Cos(\Omega t)}{2d^2}(r^2 - 2z^2) \quad . \tag{3.1}$$

The d in Eqn. 3.1 is defined by $d^2 = r_0^2 + 2z_0^2$, where r_0 is the distance from the center of the trap to the ring electrode and z_0 is the distance from the center to an endcap electrode. In our case, the signal applied to the endcap electrodes is pure AC, so U_0 can be neglected in what follows. For a particle with mass M and charge Q, this potential results in an equation of motion,

$$\frac{\partial^2 u}{\partial t^2} + (a_u - 2q_u \Omega t)u = 0 \quad , \tag{3.2}$$

where $u = x, y$, or z, $a_x = a_y = -2a_z = -4QU_0/Md^2\Omega^2 = 0$ and $q_x = q_y = 2q_z = 2QV_0/Md^2\Omega^2$ [25]. The parameters a_u and q_u are known as stability parameters because their values determine whether or not the trap will be stable in all three directions. Figure 3.3 shows the first stability region in terms of a_u and q_u. There other stable regions in $a_u - q_u$ space, but they do not intersect the $a_u = 0$ line. In the ideal case, with $a_u = 0$, the trap is stable for $0 < 2QV_0/Md^2\Omega^2 < 0.908$ [27]. In our trap, the geometrical scale d^2 is not easily defined, but the distances involved imply $d^2 \approx 10^{-4}\ m^2$.

The stability region can be used to determine a particle's charge-to-mass ratio. This is done by adjusting either the AC voltage or the trap frequency until q_u leaves the stability region. However,

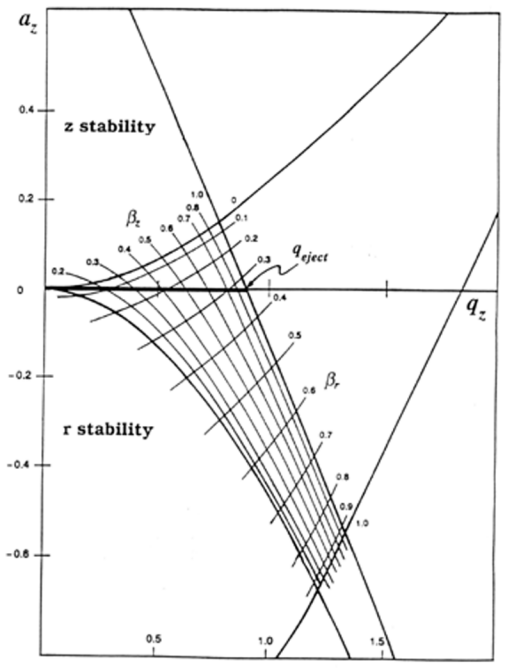

Figure 3.3: First stability region for an ideal Paul trap. Trap is stable in all three directions in the hatched region. (citation needed)

in our trap the geometrical parameter is not well known and, as shown in Sec. 3.1.2, background gas at atmospheric pressure alters the stability region. For these reasons, a rough estimate for Q/M of the silica particles in our experiment is obtained using the average size of these particles and the average electric field necessary to cancel the force of gravity. This electric field is produced by applying voltages to electrodes that sit 10 mm above and below the center of the ion trap. The center of the trap is slightly shielded from these electrodes, so the charge-to-mass ratio calculated below will be an approximate minimum for the true average value. The average silica sphere in these experiments has a radius $r = 3$ μm, which gives a mass $M = 2.5 \times 10^{-13}$ kg. Meanwhile, the average voltage applied to top and bottom electrodes is approximately ± 50 V. The electric field at the center of the trap, due to this average potential, is calculated using a COMSOL model of the electrode geometry and is found to be $E_y \approx \pm 3 \times 10^3$ V/m. Solving for Q gives $Q \approx \pm 8 \times 10^{-16}$ C $= \pm 5 \times 10^3$ e. The AC potential typically used our experiment has $V_0 = 2$ kV and $\Omega = 1.5$ kHz,

which gives $q = 2QV_0/Md^2\Omega^2 = 0.03$ using $d^2 = 10^{-4}$ m^2.

This estimate and the use of a pure AC potential on the endcap electrodes imply that our trap is operating in the limit of small a and q values, $a, q << 1$. In this limit, the solution to the particle's motion simplifies to

$$u_i(t) = A(1 - \frac{q_i}{2}Cos(\Omega t))Cos(\omega_i t) \tag{3.3}$$

for $\omega_i \approx \sqrt{(a_i + q_i^2/2)}(\Omega/2)$ [25]. This gives estimates for our trap frequencies of $\omega_{x,y} \approx 16$ Hz and $\omega_z \approx 8$ Hz.

3.1.2 Gas damping in ion traps

The analysis given above starts from an equation of motion that does not include a damping term. We have found that, for that the same charge-to-mass ratio, there is a large variation in the trap-behavior of charged silica microspheres and this variation is correlated with the sphere's diameter. For example, for the same value of Q/M, 5 μm beads will be stably trapped while 500 nm beads will drift out of the trap over extended periods of time. This implies that the effect of damping on the ion trap's operation is important, especially because the ion trap is used to initially catch beads at atmospheric pressure.

Pearson et al. [27] studied the effects of damping on micron scale spheres in ion traps. They found that the inclusion of a damping term into the Mathieu equations (Eqn. 3.2),

$$\frac{\partial^2 u}{\partial t^2} + b\frac{\partial x}{\partial \tau} + (a_u - 2q_u\Omega t)u = 0 \quad , \tag{3.4}$$

increased the region of stable trapping ($b = (12\pi\eta R)/(C(N_{kn}m\Omega))$. At atmospheric pressure, $C(N_{kn}) \approx 1$. The increased stability of the trap in the presence of damping is confirmed by numerically solving the damped Mathieu equations. Figure 3.4 shows the transition from a stable to unstable trap, in the non-damped case, for different values of q and with $a_u = 0$. The trap becomes unstable above $q = 0.908$ as expected. Figure 3.5 shows the same transition when the effects of damping are included, using a silica microsphere with radius $r = 5$ μm. Here the trap

remains stable for values of q out to 2.2. These calculations are done in the limit of small Reynolds and Knudsen numbers, which are good approximations at atmospheric pressure for the particle sizes involved.

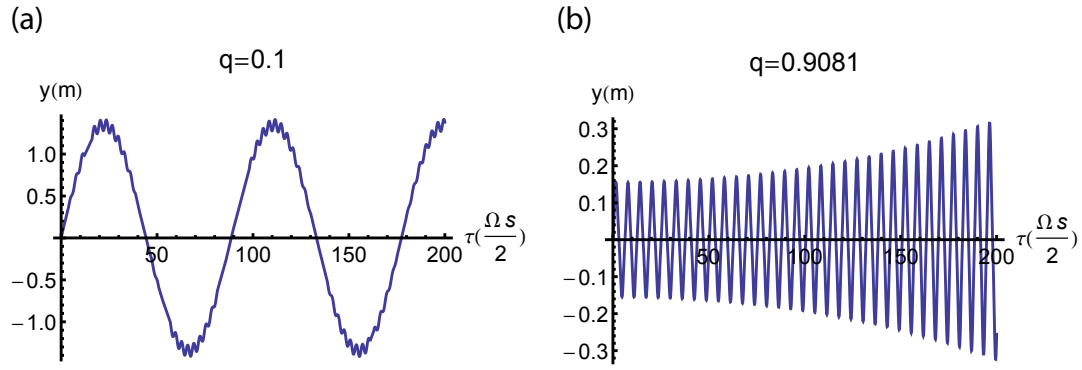

Figure 3.4: Calculation of the stability of trapped particle for $q = 0.1$ and $q = 0.9081$ without damping. Initial conditions are $y(0) = 1$ mm and $v_y(0) = 0$. The trap grows unstable for q values above 0.908.

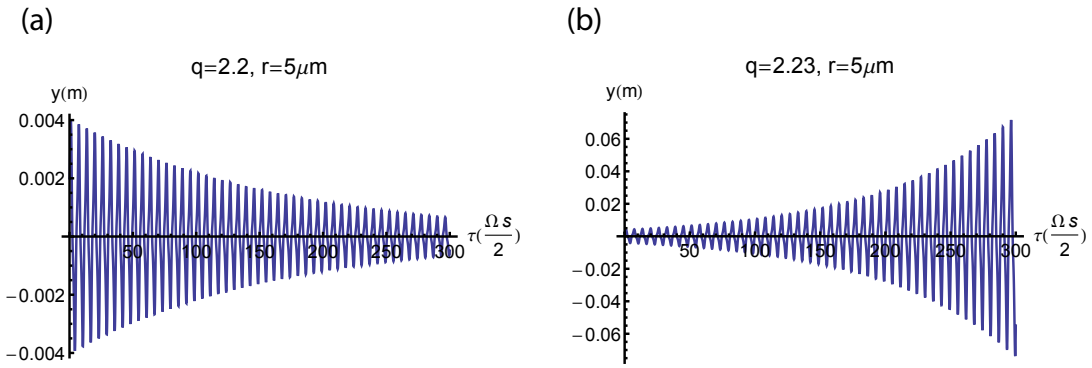

Figure 3.5: Calculation of the stability of trapped particle for $q = 2.2$ and $q = 2.3$, with damping, for a bead with a 5 μm radius at atmospheric pressure. Including a damping term in the Mathieu equations increases the region of stability. Initial conditions are $y(0) = 1$ mm and $v_y(0) = 0$.

These calculations and the work done by Pearson et al. definitely imply that damping due to background gas can influence the stability of the trap, but in our case these results do not agree with the observed behavior of particles with different damping factors— smaller particles, with larger damping factors, but the same value of Q/M are not stably trapped. However, we find that if we into account our extremely over-damped system in combination with a few effects that are not taken into account by the damped Mathieu equations, we can understand the observed experimental behavior. Figure 3.6 compares a full calculation of the motion of a 10 μm particle and a 1 μm particle at atmospheric pressure, when the particles are displaced 2 mm from the center of the trap. For the 10 μm particle, the system is over-damped and the position settles to the center of the trap on the order of 5 seconds. In the extremely over-damped case with a 1 μm particle (b), the particle's average position does not change more than a micron in around 13 s. This is compared to the 8 μm in drift expected from brownian motion, and the 17 μm in drift caused by an extra 1 V DC voltage applied to the upper and lower electrodes. Most likely, all three of these distance scales are dwarfed by the drift expected from air currents inside the vacuum chamber. So while a 0.5 μm particle is stably trapped according to the damped Mathieu equations, the above analysis implies that the particle will tend to drift out of the trap.

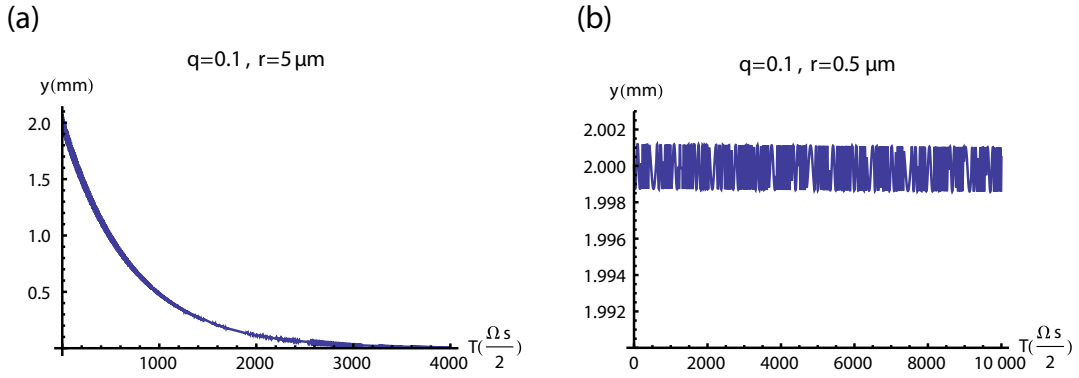

Figure 3.6: Comparison of the motion of a 10 μm particle and a 1 μm particle in an ion trap. Initial conditions are $y(0) = 2$ mm and $v_y(0) = 0$.

The ion trap is useful because it provides an easy mechanism for loading an optical trap and in a drop-recapture experiment, it would provide this same functionality. One might wonder if an optical trap is really needed, or if it would be possible to cool a mesoscopic object to the ground state of an ion trap. While the ion trap has a few advantages in terms of ease of use, an optical trap is preferable for the eventual cooling experiment. The ion trap has a driving force which cannot be ignored in solving a particle's equation of motion (oscillations of the electric field in an optical trap are probably negligible for this experiment). This means that the forces of the ion trap on the particle are not conservative, and small perturbations can lead to a lot of energy being added to the system. This is observed at low pressure, where vibrations in our optical table cause trapped particles to oscillate for timescales greater than that expected for the given damping rate. The ion trap also has a much lower frequency than that obtainable in an optical trap (Hz vs. kHz). For lower trap frequencies, a lower temperature is required to reach the quantum regime.

3.2 Optical traps

Optical traps, like ion traps, rely on an inhomogeneous, oscillating electric field. In an optical trap, the frequencies involved are much higher, so the trapped particle's center-of-mass motion depends only of the time-averaged value of the electric field. Optical traps depend on the dielectric properties of the trapped object. Depending on the size of the object and the wavelength of light used, the trapping mechanism can be described in a few different ways. For particles whose size is much larger than the wavelength of light, the trapping forces can be described by ray optics. For a particle much smaller than the wavelength, the particle can be treated as a point dipole and trapping potential arises from the interaction of the dipole moment and the gradient of the electric field. In the middle, when the particle's diameter is of the order of the wavelength of light, Lorentz-Mie theory is needed to describe the interaction of light and particle [28].

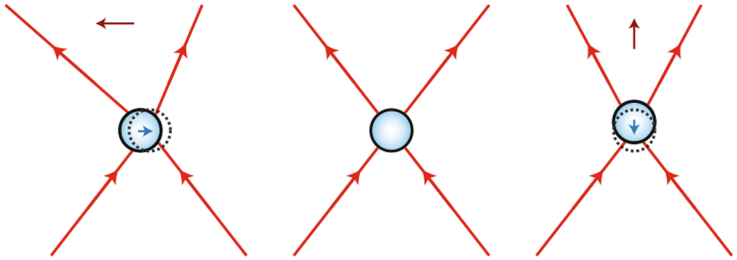

Figure 3.7: The ray optics view of optical trapping forces. The change in the light's momentum is balanced by a change in the particle's momentum. Momentum changes for the light beams are given by red arrows. Momentum changes for particle are given by blue arrows, and dotted circles represent the beam waist. Image from [28].

3.2.1 Ray optics regime

The ray optics approach to optical traps can be used to calculate the optical forces on a trapped particle, but here only the qualitative aspects of the large particle regime will be considered. Rays incident on a dielectric particle will bent at an angle that depends on the index of refraction of the particle. When the particle is displaced in a certain direction from the beam waist of a focused laser, it will refract more light in the direction of displacement. As a result, the momentum of the light field in that direction is increased and this change in momentum is balanced by an equal and opposite change in the particle's momentum. This process is depicted in Fig. 3.7.

3.2.2 Rayleigh regime

Alternatively, for particles much smaller than the wavelength of light, the optical trap can be described in terms of the dipole moment of the particle and the gradient of the electric field. The regime in which the point-dipole approximation of light-particle interaction is valid is known the Rayleigh scattering regime. Although this approximation is not valid for the $3 - 10$ μm silica particles used in this experiment, the calculations in this regime are significantly easier and are useful for understanding the functional dependence of the parameters involved.

In this regime, the instantaneous force of an inhomogenous electric field on the approximately

infinitesimal dipole is related to $\triangle\mathbf{E} = (\mathbf{d}\cdot\nabla)\mathbf{E}$, the infinitesimal change in the electric field over the length of the dipole ($\mathbf{d}$ is the infinitesimal displacement vector of the dipole). This gives a gradient force on the dipole,

$$\mathbf{F} = (\mathbf{p}\cdot\nabla)\mathbf{E} \quad [29]. \tag{3.5}$$

In order to obtain a value for $\mathbf{p}$, the approximation is taken one step further and it is assumed that the variation in $\mathbf{E}$ is significantly small over the volume of the dielectric particle such that dipole moment may be written as

$$\mathbf{p}(\mathbf{r},t) = 4\pi\epsilon_0 a^3 \left(\frac{n^2-1}{n^2+2}\right)\mathbf{E}(\mathbf{r},t) \quad [30]. \tag{3.6}$$

In Eqn. 3.6, a is the radius of the particle, n is the index of refraction, $\mathbf{E}(\mathbf{r},t)$ is the electric field evaluated the center of the particle, and it is assumed that the medium surrounding the particle has index of refraction $n_0 = 1$. The force we are interested in is not the instantaneous force of Eqn. 3.5, but the force averaged over an oscillation of the electric field. This force can be written as

$$\mathbf{F}_{grad}(\mathbf{r}) = \frac{2\pi a^3}{c}\left(\frac{n^2-1}{n^2+2}\right)\nabla I(\mathbf{r}) \quad . \tag{3.7}$$

The intensity near the waist of a Gaussian beam can be approximated as

$$I(\mathbf{r}) = \left(\frac{2P}{\pi w_0^2}\right)\frac{1}{1+(2\tilde{z})^2}\exp\left[-\frac{2(\tilde{x}^2+\tilde{y}^2)}{1+(2\tilde{z})^2}\right] \tag{3.8}$$

where P is the beam power, $(\tilde{x},\tilde{y},\tilde{z}) = (x/w_0, y/w_0, z/kw_0^2)$, and $k = 2\pi/\lambda$. This leads to a harmonic trap with angular trap frequencies

$$\omega_{x,y}^2 = \frac{8\pi a^3}{mc}\left(\frac{n^2-1}{n^2+2}\right)\left(\frac{2P}{\pi w_o^4}\right) \tag{3.9}$$

$$\omega_z^2 = \frac{2\pi a^3}{emc}\left(\frac{n^2-1}{n^2+2}\right)\left(\frac{8P}{\pi k^2 w_o^6}\right) \tag{3.10}$$

for beam waist w_0 and z taken as the direction of beam propagation [30]. It is nice to have analytic expressions for the trap frequencies, but these expressions were derived under the assumption of $a << \lambda$ which is not valid in our experiment. Y. Harada and T. Asakura [30] used generalized

Lorentz-Mie theory to study the application of the Rayleigh regime results to spheres with diameters similar to the wavelength of light. They found that in the radial directions, these approximations are valid as long as the particle is smaller than the beam waist. They also found that the approximation for the axial direction broke down at smaller particle sizes than for the radial directions. In our experiment, the beam waist is 3 μm, while the silica spheres have diameters from $3 - 10$ μm. Li [28] also studied the generalized Lorentz-Mie theory for micron scale spheres. He found that for spheres with diameters similar to the wavelength of light, only particular sphere sizes can be stably trapped. This is attributed to interference effects between the light scattered by the particle and that not scattered.

3.2.3 Scattering and perturbing forces

The gradient force is responsible for the trapping potential, but a laser beam produces other forces on dielectric particles. There is a scattering force, which pushes the particle in the direction of beam propagation. In the Rayleigh regime this force is proportional to a^6, while from Eqn. 3.7, it is apparent that the gradient force is proportional to a^3, so this force is more important for larger particles.

Along with the scattering forces, there are also forces which arise from the perturbations caused by mechanical vibrations and power fluctuations of the trapping laser. At atmospheric pressure, the perturbations from these sources are quickly damped out, but at lower pressures the perturbations lead to instabilities [31]. In order to trap particles at pressures for which optical traps are unstable, feedback is needed to damp out large, spontaneous oscillations. So far, experiments with optical traps at low pressure have applied this feedback using a variety of techniques. Ashkin and Dziedzic [31] originally designed a feedback system using position detection along the beam axis and an electro-optic modulator to control the laser power. More recently, Li, Kheifets, and Raizen used a feedback system consisting of three extra laser beams whose scattering force was controlled by acousto-optic modulators [16]. In another experiment, J. Gieseler et al. [17] demonstrated three-dimensional feedback with an elliptic beam and parametric feedback— they changed the trap

stiffness in response to the particle's position in the potential well. In our experiment, a group of electrodes surrounding the optical trap are used to apply electric forces to the trapped particle.

Chapter 4

Equations of motion in a harmonic trap

The behavior of a particle in an optical or ion trap (ignoring micromotion) is described by brownian motion in a harmonic potential. On short timescales, the time-domain signal of the motion is not easily analyzed. In order to glean useful information, such as the center-of-mass temperature or damping factor, it is necessary to analyze the Fourier transform of the particle's motion over an extended period of time. This frequency-domain information is obtained in the form of the particle's power spectral density. This chapter describes the motion of a particle in a harmonic trap when including the effects of damping from the background gas and random collisions with the gas molecules.

4.1 Langevin equation

The Langevin equation for one dimension of a harmonic potential [32] is

$$m\ddot{x} + \gamma_0\dot{x} + kx = (2k_B T_0 \gamma_0)^{1/2}\eta(t) \tag{4.1}$$

where $x(t)$ is the position of the particle, m is the mass, γ_0 is the friction coefficient, k is the trap stiffness, and $(2k_B T_0\gamma_0)^{1/2}\eta(t)$ is a white noise driving force for a gas at temperature T_0 that satisfies the criteria,

$$\langle \eta(t) \rangle = 0 \tag{4.2}$$

$$\langle \eta(t)\eta(t') \rangle = \delta(t - t') \quad . \tag{4.3}$$

The form of the driving force implies that the collisions with gas molecules are assumed to be completely elastic. This equation breaks up the effects of the background gas on the particle into

two terms— the γ_0 term describes the time averaged effect (damping), while $\eta(t)$ is responsible for the random Brownian forces. At atmospheric pressure, the viscous damping factor $\Gamma_0 = \gamma_0/m$ is given by Stoke's law, but at lower pressures the approximation of small Reynolds and Knudsen numbers breaks down and a correction term is needed,

$$\Gamma_0 = \frac{6\pi\mu r}{m}\frac{0.619}{0.619 + Kn}(1 + c_K) \quad [16]. \tag{4.4}$$

In this expression, $\mu = 18.27$ μPa·s is the dynamic viscosity coefficient of air at room temperature, r is the particle radius, Kn is the Knudsen number, and $c_k = (0.31Kn)/(0.785 + 1.152Kn + Kn^2)$.

Equation 4.1 can be solved in terms of the power spectral density of the particle's motion,

$$S_x(\omega) \equiv \lim_{t_T \to \infty} \frac{2}{t_T}|x(\omega)|^2 \quad \text{for} \tag{4.5}$$

$$x(\omega) = \frac{1}{\sqrt{2\pi}}\int_{-t_T/2}^{t_T/2} x(t)e^{-i\omega t}dt \quad . \tag{4.6}$$

Using the identity $\int_{-\infty}^{\infty}|x(\omega)|^2 d\omega = \int_{-\infty}^{\infty}|x(t)|^2 dt$, one can see that $\int_0^{\infty} S_x(\omega)d\omega = \langle x(t)^2\rangle$. The equipartion theorem implies that the temperature T_0 in Eqn. 4.1 is

$$T_0 = \frac{m\omega_0^2}{k_B}\langle x(t)^2\rangle \tag{4.7}$$

where w_0 is the trap frequency. In terms of the power spectral density, the solution to Eqn. 4.1 is

$$S_x(\omega) = \frac{2k_B T_0}{m}\frac{\Gamma_0}{(\omega_0^2 - \omega^2)^2 + \omega^2\Gamma_0^2} \quad [16]. \tag{4.8}$$

4.2 Feedback and measurement

Equation 4.8 describes a particle's behavior in a harmonic trap with a background gas at temperature T_0. In our experiment, active feedback is used cool the center-of-mass motion and also increase the trap frequencies. Cooling is accomplished with derivative feedback, which is applied by sending a 90° phase-shifted signal of the particle's motion along one axis to the electrodes controlling position along that axis. This feedback changes the effective temperature of the particle's motion by increasing the damping factor $\Gamma_{tot} = \Gamma_0 + \Gamma_{fb}$. Neglecting the noise involved in measurement

and feedback, the temperature of the feedback damping reservoir is approximately 0 K and the effective temperature is given by

$$T_{eff} = \frac{\Gamma_0 T}{\Gamma_{tot}} \quad [4]. \tag{4.9}$$

With derivative feedback, the temperature and damping terms in the power spectrum are replaced by their new effective values and the shape of the spectrum changes accordingly. These changes can be used to determine temperature information for a cooled particle.

It is also possible to change the frequency of the trap using active feedback. This is done by applying proportional feedback— sending a signal to the feedback electrodes which is 180° out of phase with the particle motion. Proportional feedback applies a force proportional to the particle's displacement from the center of the trap. This is simply increases the trap stiffness, resulting in a higher trap frequency. Figure 4.1 shows the power spectrum in a harmonic trap with different amounts of proportional and derivative gain. All of the relationships derived above ignore the effects of measurement error. Appendix D contains information interpreting the power spectrum in the presence of measurement error.

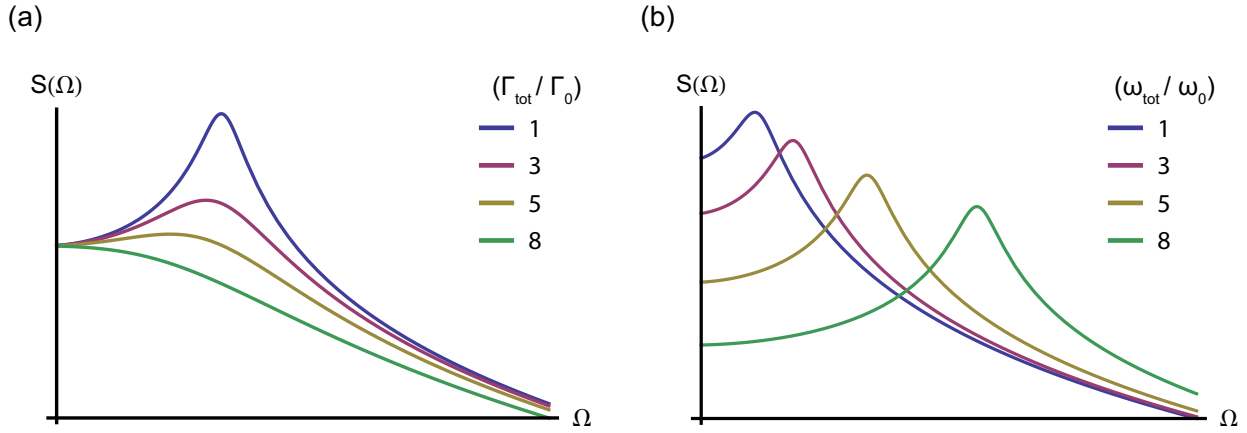

Figure 4.1: (a) Power spectrum with varying amounts of derivative gain. (b) Power spectrum with varying amounts of proportional gain.

Chapter 5

Experimental apparatus

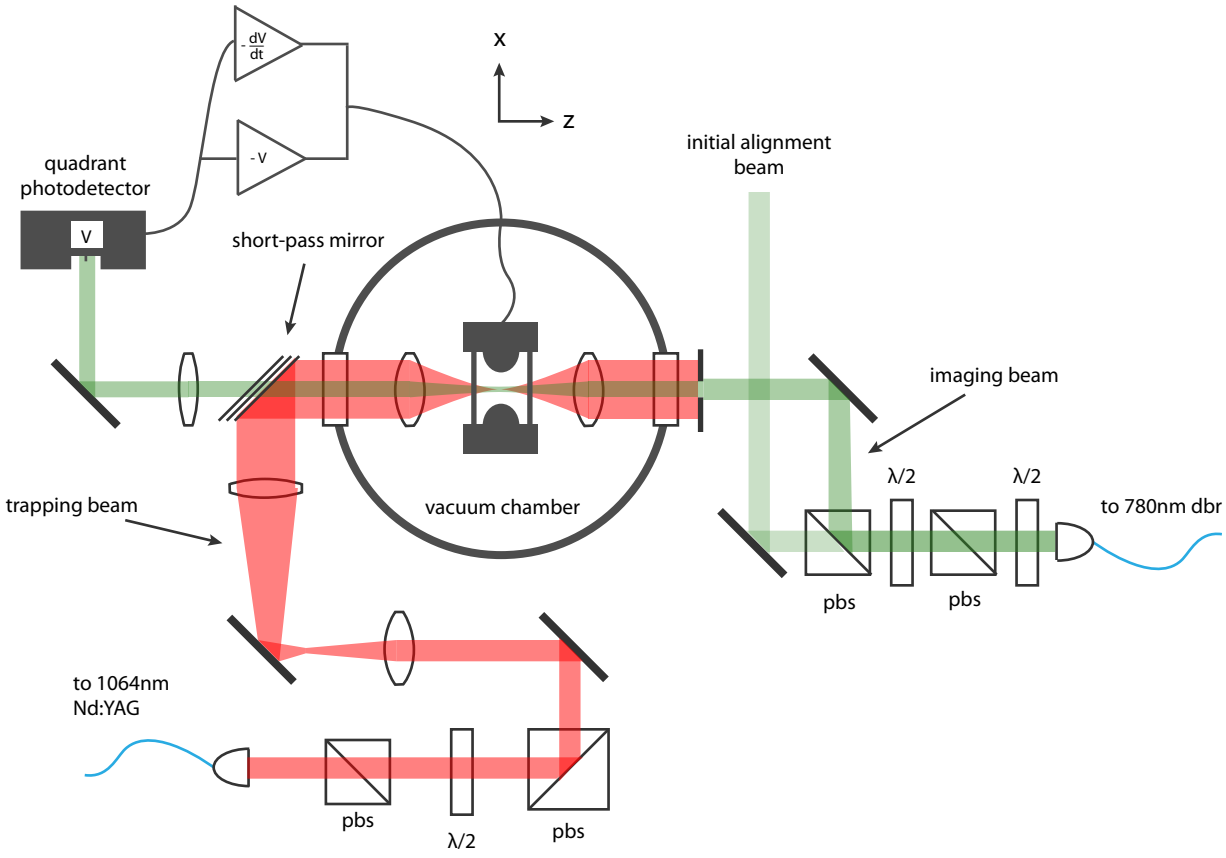

Figure 5.1: The trapping beam has a wavelength of 1064 nm with power up to 150 mW, focused to a beam waist of 3 μm. The particle position is detected using a beam with wavelength 780 nm, focused to a waist of approximately $w_0 = 20$ μm. A 500 mm focal length lens creates a 20$\times$ magnified image of the particle on a quadrant photodetector. The signal of from the photodetector is sent to analog derivative and proportional feedback circuits with variable gain. Electrodes surrounding the optical trap are used to apply feedback to the trapped particle.

5.0.1 Paul trap and feedback electrodes

The experimental apparatus was designed with the goal of testing a hybrid ion-optical trap. The AC paul trap electrodes and the optical trap lens all reside in a cylindrical vacuum chamber approximately 30 *cm* in diameter and 15 *cm* tall. The Paul trap (Fig. 5.2) was modeled after a trap designed by C. Alvarez [18], which in turn was based on a design by Schlemmer, Illemann, Wellert, and Gerlich [33]. The current trap is constructed with 8 rods for manipulation of the particle in the x and y directions and two ring-shaped electrodes, placed around the AC cones, serve to manipulate the particle's motion in the x direction. The geometry of these electrodes was developed to allow for three-dimensional feedback a trapped particle's position. The silica particles are $3 - 10$ μm spheres manufactured by Corpuscular Microspheres-Nanospheres. They acquire charges when in injected into the vacuum chamber with a plastic syringe.

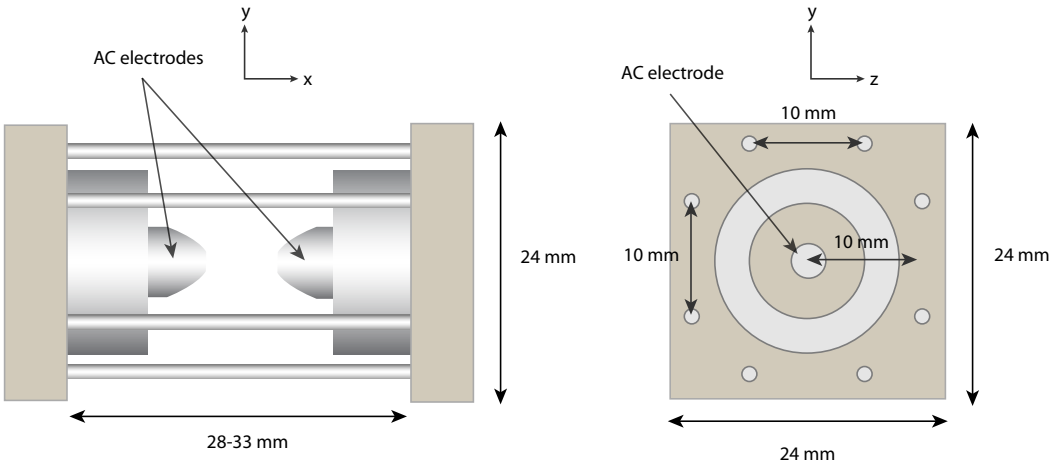

Figure 5.2: The endcaps are the two cone-shaped electrodes at the center of the trap. The other electrodes are used to manipulate the particle's position. Note that the here the coordinate system is labeled with respect to the optical trap and so comparison with the Mathieu equations of Ch. 3 requires a permutation of the axes.

The x feedback electrodes are partially shielded by the inner AC electrodes. The shape of

these electrodes and the shielding produce an electric field which has components in the y and z directions, especially at locations displaced from the geometrical center of the trap. This introduces some feedback-coupling between the axes. In the long-term, the configuration of these electrodes may limit the amount of cooling possible. Li, Kheifets, and Raizen [16] found that their minimum obtainable temperature was limited by coupling between motion along different axes. In their case, this coupling was the result of slight beam deflections caused by the AOM's used to manipulate the particles. One way around this problem would be to apply the x feedback signal directly to the AC electrodes.

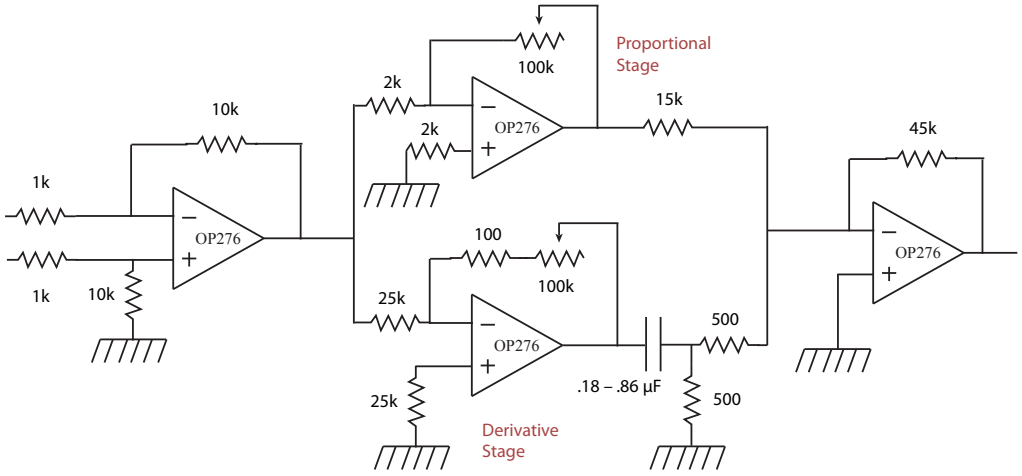

Figure 5.3: Feedback circuitry for one axis.

As seen in Fig. 5.1, the position measurement system consists of 25 mm and 500 mm focal length lenses that project a 20× image of the particle onto a quadrant photodetector. Position detection in the z direction relies only on the scattered light from the particle in the optical trap. An imaging system on top of the vacuum chamber projects an image of the trapped particle onto a split mirror and light from the split portions of the image is collected and focused onto two photodetectors. Signals from the three respective axes are sent through analog derivative and proportional feedback circuits, each with variable gain. The proportional feedback circuits are

variable-gain, inverting amplifiers. The derivative circuits are variable-gain, inverting amplifiers in conjunction with high pass filters. When the cut-off frequency of the high-pass filters is much higher than the frequency of particle motion, these derivative circuits produce a signal which is 90° out of phase with the input signal. Figure 5.3 shows a circuit diagram for one axis of feedback.

5.0.2 Optical trap

The sizes of the particles used in the experiment are such that the gradient force along the z-axis of the optical trap is dominated by the scattering force. In order to trap particles in the optical trap, this scattering force must be counteracted. This can be accomplished by two different methods, each which has certain disadvantages. The first method is to apply a DC voltage to the z positioning electrodes. This method has the disadvantage that the particle is easily lost in the initial alignment of the trap. The other method consists of using two, counter-propagating beams (Fig. 5.4). This method has the advantage that the scattering forces from the two beams cancel, but the initial alignment of the beams is challenging. For both methods, the traps are formed using 25 mm focal length, 11.4 mm clear aperture lenses which are approximately uniformly filled with 1064 nm light. This forms a diffraction-limited beam waist of 2.8 μm.

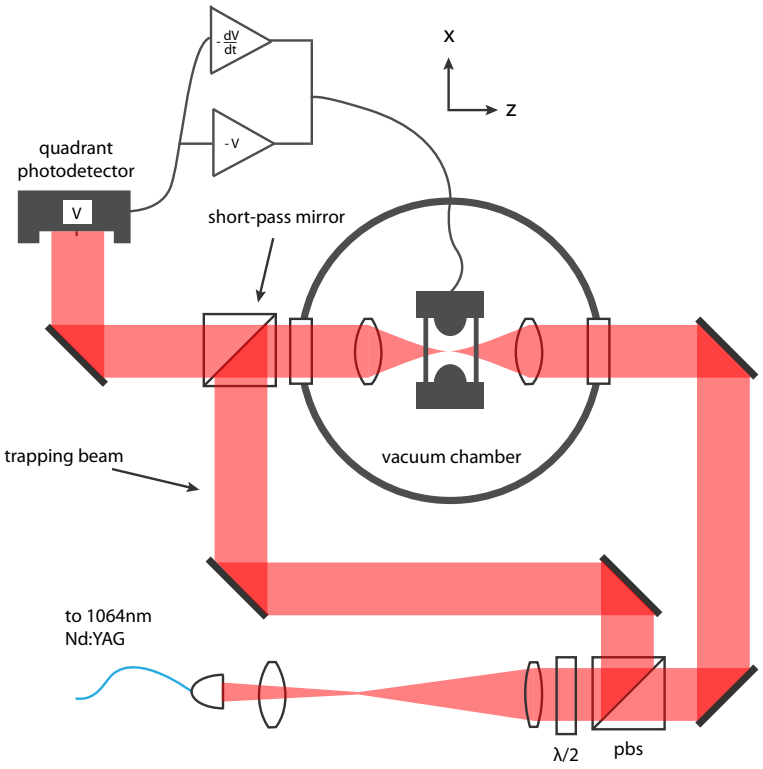

Figure 5.4: Two-beam optical trap. In a two-beam trap, scattering forces from counter-propagating beams cancel. Position detection in this setup does not use an image of the bead. Instead, deflection of the beam by the particle is directly measured by the quadrant photodetector.

Chapter 6

Results

6.1 Optical trap at atmospheric pressure

Using the trapping and measurement arrangement shown in Fig. 5.1, the power spectrum was measured along each axis of the trap for a silica particle at atmospheric pressure. Figure 6.1 shows the power spectrums along each axis of an optical trap both with and without feedback applied. The feedback consisted of both derivative and proportional terms. The data are given in units of V^2Hz^{-1}, and so require an unknown calibration factor to get to the more meaningful units m^2Hz^{-1}. However, if it is assumed that the center-of-mass temperature without feedback is approximately room temperature (297 K), some temperature information can be calculated from this data. From Eqn. 4.7, it is apparent that the ratio of temperatures for two different spectrums (with the same calibration factor β) is

$$\frac{T}{T_0} = \frac{\omega^2\langle x(t)^2\rangle}{\omega_0^2\langle x_0(t)^2\rangle} = \frac{\beta\omega^2\langle x(t)^2\rangle}{\beta\omega_0^2\langle x_0(t)^2\rangle} \quad . \tag{6.1}$$

For the x and y axes of the trap, this equation has been used to determine the approximate temperatures for the particle with feedback. In the x-direction, the temperature is calculated as 230 ± 30 K. In the y-direction, the calculation gives a temperature of 330 ± 40 K. In the z-direction, the trap frequency without feedback is very low, and the power spectrum cannot be fit easily. This means that no temperature information for the z axis can be obtained from this data— even though the area under the data can be calculated numerically, the value of ω_0 is unknown. The calculated damping factors for the x and y axes with feedback are $\Gamma_{tot,x} = 8.6\Gamma_0$ and $\Gamma_{tot,x} = 9.5\Gamma_0$, which imply temperatures $T_x = 35$ K and $T_y = 31$ K. The discrepancy between the temperatures expected

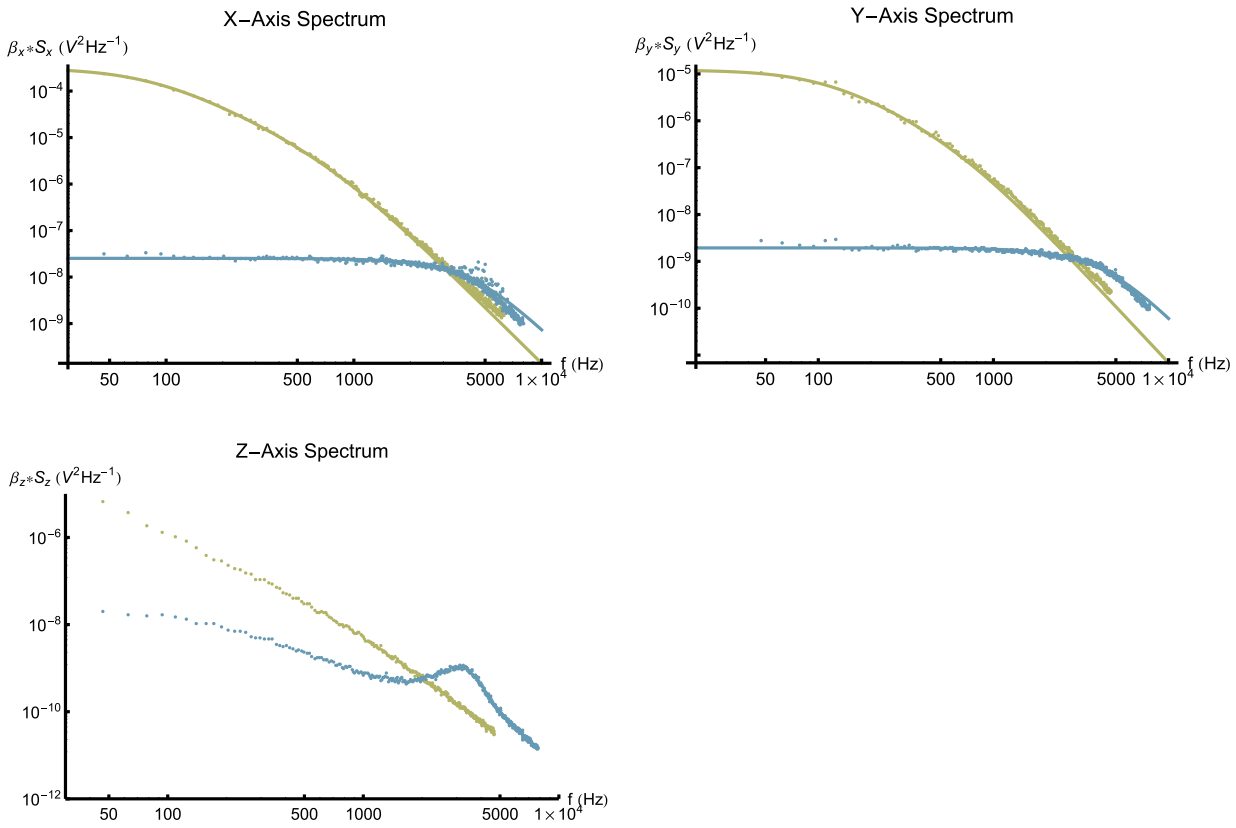

Figure 6.1: Power spectrums for three axes of an optical trap at atmospheric pressure. Blue data are without feedback, purple data are with both proportional and derivative feedback. The trapping beam power is 22.1 mW and the calculated particle radius is 2.6 ± 0.1 μm. Assuming that the particle's center-of-mass is initially at 297 K, the temperature with feedback can be calculated based on a comparison of the areas under the fit curves.

based on the damping factors and those observed indicates that the feedback for this data set was not behaving ideally.

There are several sources which could be contributing to the rise in temperature (see Appendix D), but most likely it is a combination of many. These sources include incorrect feedback phase, feedback coupling between axes, and feedback of measurement noise. These data do not display the ideal feedback one would like for this experiment, but they do demonstrate the ability

manipulate a trapped particle's position in all three dimensions of the trap. As a consistency check, these data can be used to calculate the radius of the trapped silica particle: $r = \sqrt{4.5\mu/\rho\Gamma_0}$, for dynamic viscosity μ and silica density ρ. Using the damping constants from fits to the x and y spectrums, this radius is found to be $2.6 \pm 0.1\ \mu m$. This radius lies within the expected range for the particles used in this experiment, $1.5\ \mu m < r < 5\ \mu m$. If particles were used which had a small size-variance, then the damping factors found without feedback could be used to calibrate the temperature.

6.2 Ion trap cooling in vacuum

The power spectrums from the optical trap at atmospheric pressure show an over-damped system. The reason this levitated particle system has been proposed for cavity optomechanics experiments is that it could provide a very under-damped system; a system that is very weakly coupled to its environment. In order to get a system like this, the experiment must be carried out in vacuum (very high vacuum to cool to the ground state). As mentioned in Chapter 3, optical traps are inherently unstable at low pressures and derivative feedback is needed when operating an optical trap at low pressure. Because of the difficulties involved in keeping a particle trapped when attempting to pump to low pressures, low pressure analysis was first carried out using a particle in the ion trap. The data obtained in the ion trap operating in the millitorr range show the benefits of doing the experiment low pressure. They also motivate the need for an optical trap.

Figure 6.2 displays y-axis power spectrums for varying amounts of derivative feedback at tens of millitorr. The power spectral densities have been calibrated using the ratio of particle displacement to signal voltage. This means that the temperatures calculated for this data set do not depend on the assumption of a 297 K starting temperature. The temperatures given in Fig. 6.2 are based on the $\langle x(t)^2 \rangle$ value obtained by integrating the fit functions. The given errors are almost entirely the result of error in the calibration measurements. It is apparent that at low frequencies these fits do not accurately reflect the data sets, so it might seem reasonable to use the value of $\langle x(t)^2 \rangle$ obtained by numerically integrating the interpolated data sets. However, the definition

of temperature used here, Eqn. 4.7, is given in terms of the frequency of a harmonic trap. The spectrums at low frequency contain features due to the micromotion of the ion trap and vibrations caused by the vacuum pump and these features make it difficult to interpret the temperatures given by the combination of numerically integrated data and trap frequencies. This problem could be fixed by operating at much higher trap frequencies, and this could be accomplished by using an optical trap with a small beam waist.

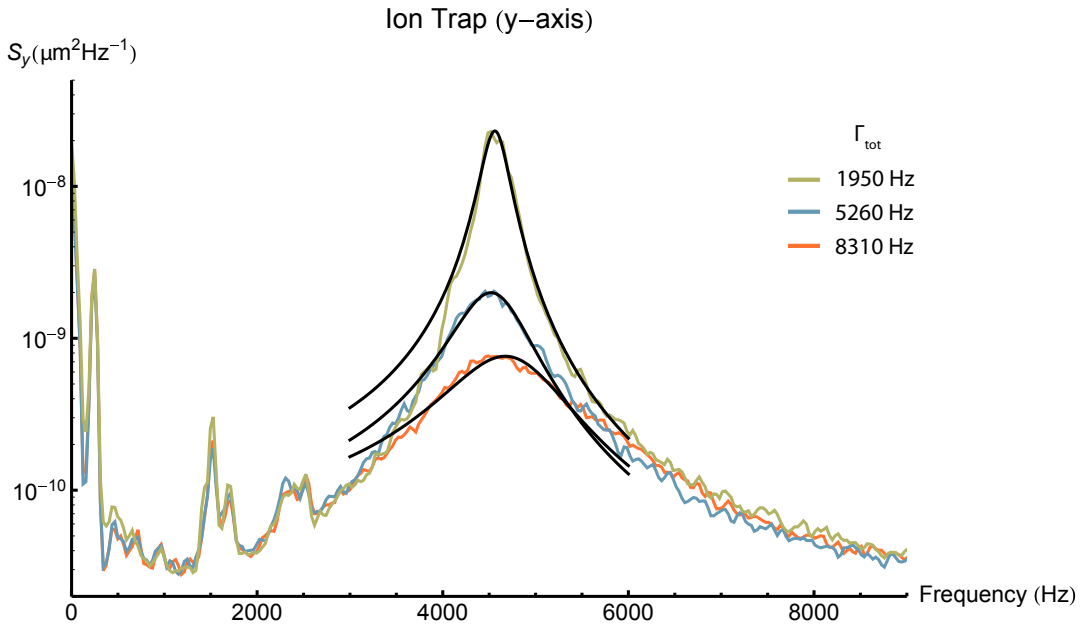

Figure 6.2: Power spectrums for the y-axis of the ion trap in the millitorr pressure range. Area under the power spectral density drops as the derivative feedback gain is increased. Spectrums are labeled by the absolutely calibrated temperatures, corresponding to the fits for each data set. The calibrated temperatures are calculated as 910 ± 100 K (green), 290 ± 30 K (blue), and 300 ± 30 K (orange).

The temperatures calculated for Fig. 6.2 show that as the derivative feedback gain is increased, the temperature drops and then begins to rise. This effect could be due to measurement noise (see Appendix D), but in this case it is most likely the result of a change in derivative feedback phase as the gain is increased. This effect was observed in the derivative feedback circuitry used in this experiment, and while it seems inherent to the design of this circuit, it can be minimized by raising

the cut-off frequency of the derivative stage's high-pass filter (Fig. 5.3). Figure 6.2 shows this gain-phase dependence for higher values of gain with the same particle and trap of Fig. 6.2.

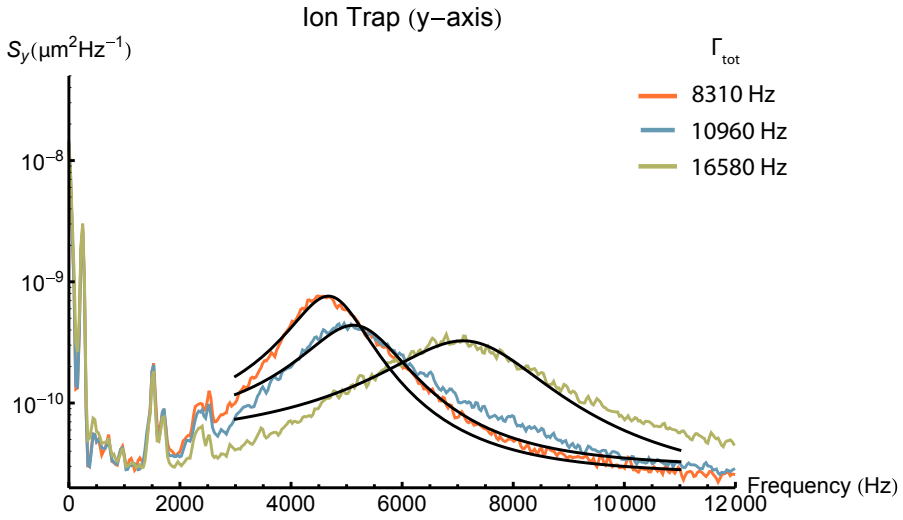

Figure 6.3: For the same particle of Fig. 6.2, at the same pressure, as the derivative feedback gain is increased even further, the phase of feedback changes. This increases the frequency of the trap and the temperature. The calibrated temperatures are calculated as 400 ± 50 K (green), 370 ± 40 K (blue), and 300 ± 30 K (orange).

It is apparent from the data with little derivative gain that was used that something in the system is heating the center-of-mass motion of the particle. Some of this heating comes from the driving forces of the ion trap and vacuum pump vibrations, but it is also the result of the phase of the proportional feedback. From Fig. 6.2, one can see that the trap frequencies involved are in the kHz range, much higher than the ion trap frequencies estimated in Sec. 3.1. These trap frequencies were obtained by applying proportional feedback. While this helped separate the secular, harmonic trap motion from the micromotion, it comes with the downside that error in the feedback phase will produce unwanted behavior. In this case, error in the proportional feedback phase decreased the damping constant and raised the temperature. Figure 6.4 displays measurements of damping factor as a function of proportional feedback for a particle trapped at atmospheric pressure. For the ion trap, this effect makes it difficult to compare the absolute calibrated temperature to that calculated by assuming a 297 K initial temperature— the power spectrum without proportional

feedback cannot be fit because of micromotion, electronic noise, and the low trap frequencies.

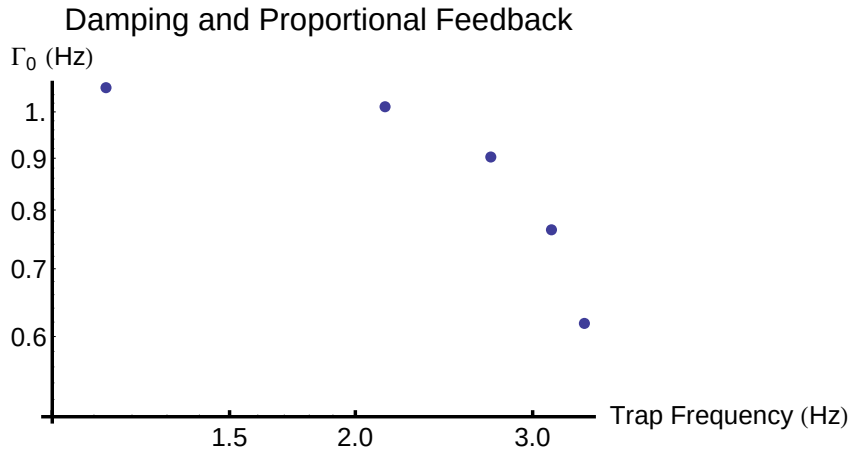

Figure 6.4: As the proportional feedback gain is increased, the damping factor decreases.

6.3 Optical trap cooling in vacuum

Optically trapping a particle at low pressure requires the use of derivative feedback because of the instabilities caused by power fluctuations of the trapping laser and the photo-thermal forces of the background gas on the particle. We have found that evacuating our chamber causes drift in our trapping and measurement beams. For this reason, alignment of the optical trap and measurement beams was carried out at 280 Torr, prior to pumping to low pressure. The data displayed in Fig. 6.5 show the power spectrum of a particle in a two-beam optical trap as the pressure is lowered. This data can be compared to the ideal, expected behavior for a harmonic trap as the ambient pressure is lowered (Fig. 6.6). It is apparent that the application of derivative feedback is changing the trap frequency even though the cut-off frequency has been raised. The same particle was trapped at even lower pressures, but the feedback amplifier began to oscillate, and this dramatically increased the temperature.

In Fig. 6.7 the spectrum at 675 mTorr is compared to the starting spectrum at 280 torr and a temperature is extracted based on the peak fit. It is apparent that the center-of-mass motion has been heated by the addition of derivative feedback, but again we see that the oscillator is not

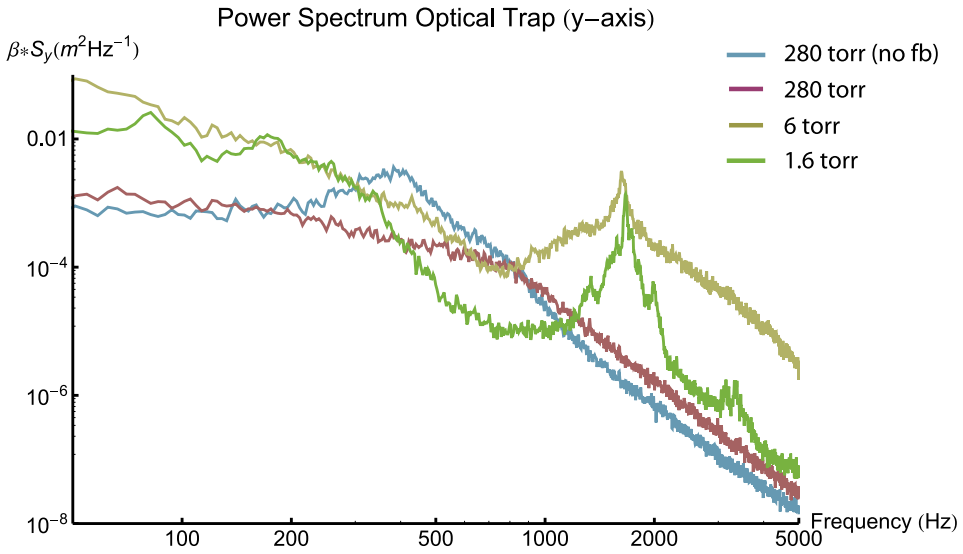

Figure 6.5: These data represent the power spectrum of a two-beam optical trap as a function of pressure. At 380 mTorr the feedback amplifiers began to oscillate, dramatically raising the temperature.

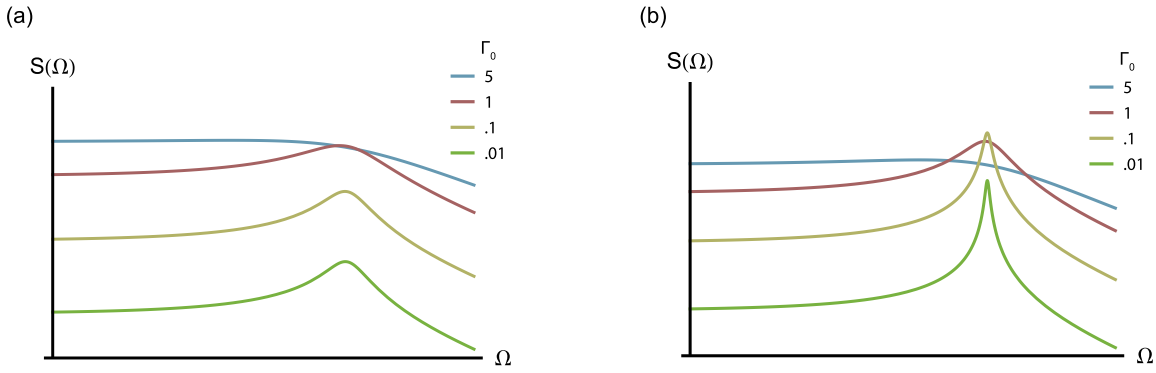

Figure 6.6: The ideal pressure dependence of the spectrum. The behavior depends on the gain of derivative feedback. (a) has $\Gamma_{fb} = 1$. (b) has $\Gamma_{fb} = 0.1$. Compare these values with the damping of the background gas (Γ_0).

over-damped at lower pressures.

The optical trap power spectrum as a function of pressure is shown for another silica microsphere in Fig. 6.8. For this data set, the bipolar amplifiers that send the feedback signal to the trap's electrodes has been replaced in order to prevent the spontaneous oscillations observed

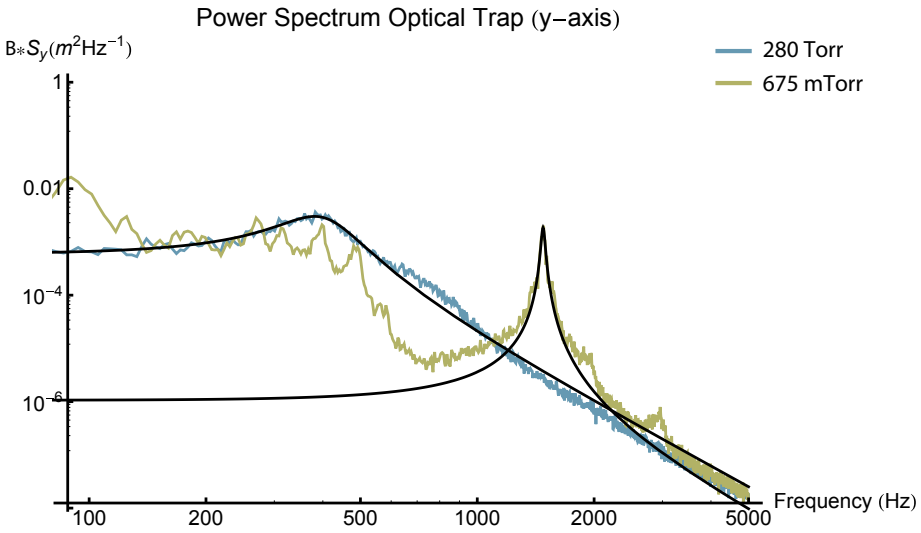

Figure 6.7: These data are power spectrums of a two-beam optical trap at 280 torr and 675 mTorr. The calculated temperature at 675 mTorr is 500 K.

previously. The trap lenses have also been translated along the z-axis in an attempt to precisely overlap the two beam waists. In this dataset, two different Lorentzian peaks begin to emerge at lower pressure. The first is centered on 1078 ± 7 Hz, while the second is at approximately 4 kHz. Examining the power spectrum without any feedback, it is clear that the true y-axis trap frequency corresponds to the first peak. The second peak appears to be related to coupling between feedback in the z direction and motion in the y direction. The second peak and the noise features at low frequency make it difficult to estimate the particle's center-of-mass temperature for lower pressures. Still, the spectrums do contain some useful information about the behavior of the particle in the optical trap. Fitting the portions of the power spectrum which correspond to thermal motion in the optical trap gives a temperature which can be thought of as the temperature of the combined gas and derivative feedback reservoir.

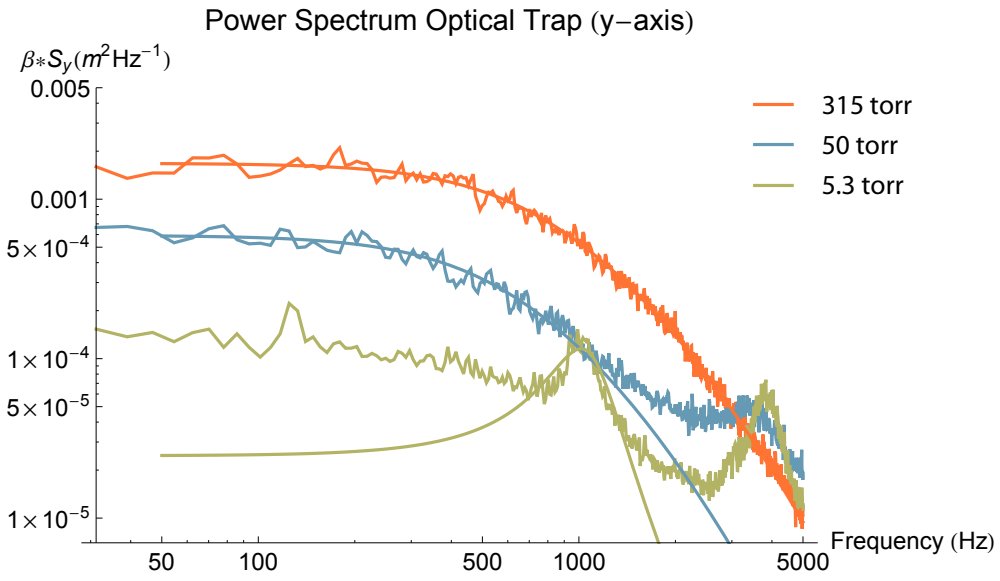

Figure 6.8: Power spectrums of a two-beam optical trap as a function of pressure (a different particle, and different bipolar feedback amplifiers than for data in Fig. 6.5 and Fig. 6.7). There are noise features below 750 Hz that are also present in the ion trap cooling spectrums. At higher frequencies, there are Lorentzian features visible, but these seem to be related to feedback coupling between the z and y axes. The temperatures relative to the temperature at 315 Torr are calculated as 79 K (purple) and 17 K (gold). These temperatures are calculated based on fits to the spectrums. These temperatures represent the thermal equilibrium between the particle and the background gas/derivative feedback.

Chapter 7

Conclusions

Attempts to cool the center-of-mass motion in both the ion and optical traps at low pressure suffer from the effects of vibrational and electronic noise for frequencies below 1 kHz. In the ion trap, these effects are exaggerated because of the driving AC fields, but they remain a problem when using the optical trap alone. One way to mitigate coupling between particle motion and low frequency noise is to use a trap with a much higher frequency. Looking at Eqn. 3.9, the two most obvious ways to increase the trap frequencies are to decrease the beam waist or to increase the beam power. This may also require decreasing the particle size to stay in a regime defined by this equation. It is clear that the trap frequencies are more sensitive to changes in the beam waist; they grow like $1/w_0^2$ in the radial direction and $1/w_0^3$ in the axial, whereas they proportional to $\sqrt{P}$. Given the high laser power currently being used in this experiment, around 130 mW, the simplest and most effective method for increasing the frequencies would be to decrease the beam waist. The trapping lenses used for the above data both have numerical apertures of 0.228. If the 1/2" trapping lenses are swapped for diffraction limited 1" lenses, the radial trap frequency can be increased by a factor of 6, while the axial trap frequency can be increased by a factor of 14.

Low frequency noise is definitely a problem with the current system, but a more fundamental issue appears to be coupling between feedback in the axial direction and motion in the radial. Some of this coupling is likely due to a misalignment of the trap and feedback axes (see Appendix D), but it could be an intrinsic feature of the trap potential [31]. Since, for small enough displacements, the trap potential will begin to appear more and more harmonic, the trap axes may be more effectively decoupled by increasing the trap depth. This implies that decreasing the beam waist could help

remove the coupling features observed in Fig. 6.8.

The issues listed above are most likely responsible for the majority of center-of-mass heating observed, but there are other features of the trap that lead to non-ideal behavior. First, the use of two trapping beams means that it is possible to produce a bistable potential. Time traces of the z-axis signal have similar features to those seen for a bistable optical trap studied by [34]. This implies that the beam waists of the two trapping beams lie at different points on the z-axis. Another non-ideal feature of the trap is related to the size of the particles used. Li [28] analyzed the trapping forces for silica spheres with sizes around the wavelength of trapping light, and found that interference effects between the light scattered by the sphere and that not scattered can lead to saddle-shaped potentials instead of stable trapping wells. This could explain the inability to load the optical trap for certain microspheres in the $3 - 10\ \mu m$ range, but it could also be related to unexpected, high frequency features in the z-axis spectrum of certain particles. This problem could be circumvented by using particles much smaller than the wavelength of light. Given that, in the Rayleigh regime, optical trapping forces are proportional to the volume of the particle, the use of smaller silica spheres would be another reason for moving to a tighter optical trap.

Thus far, this experiment has been mostly an exploration into the use of a hybrid ion-optical trap and a particular feedback system. While following closely in the footsteps of similar experiments [35, 16, 17], our apparatus uses a different type of stabilization feedback that consists of a series of electrodes surrounding the trap. While this system has problems related to the misalignment of the trap and feedback axes, these problems do not seem to be an inherent feature of this type of feedback. Given a different geometry of electrodes, the feedback coupling between axes could be effectively eliminated. This is not the case, for example, when using AOM's to control the optical forces on a trapped particle or when changing the trap stiffness in all three directions in response to the signal along one axis. The coupling between axes in both these techniques seems to be intrinsic to the feedback method.

The apparatus and experiment described here are the first steps towards the ground state cooling of a levitated silica particle. Once a feedback system is in place that allows for the stable

trapping of a particle in high vacuum, this apparatus can be placed inside of an optical cavity and the methods described in Sec. 2.4 can be used to further cool the motion of the particle.

Bibliography

[1] Kippenberg, T. J. & Vahala, K. Science **321**, 1172 (2008).

[2] Kippenberg, T. J., Rokhsari, H., Carmon, T., Scherer, A. & Vahala, K. J. Phys. Rev. Lett. **95**, 033901 (2005).

[3] Arcizet, O., Cohadon, P. F., Briant, T., Pinard, M. & Heidmann, A. Nature **444**, 71 (2006).

[4] Poggio, M., Degen, C. L., Mamin, H. J. & Rugar, D. Phys. Rev. Lett. **99**, 017201 (2007).

[5] Lechner, W., Habraken, S. J. M., Kiesel, N., Aspelmeyer, M. & Zoller, P. Cavity optomechanics of levitated nano-dumbbells: Non-equilibrium phases and self-assembly (2012). Oai:arXiv:1212.4691.

[6] (LIGO), G. M. H. Class. Quantum Gravity **27**, 084006 (2010).

[7] Teufel, J. D. Nature **475**, 359–363 (2011).

[8] Chan, J. et al. Nature **475**, 89–92 (2011).

[9] Purdy, T. P., Peterson, R. W. & Regal, C. A. Science **339**, 801 (2013).

[10] Zurek, W. H. Phys. Today **44**, 0031–9228 (1991). [updated version, 2003, arXiv:quant-ph/0306072v1].

[11] Marshall, W., Simon, C., Penrose, R. & Bouwmeester, D. Phys. Rev. Lett. **91**, 13 (2003).

[12] Kleckner, D. et al. New J. Phys. **10**, 095020 (2008).

[13] Penrose, R. Gen. Rel. Grav. **28**, 581–600 (1996).

[14] Chang, D. E. et al. PNAS **107 (3)**, 1005–1010 (2008).

[15] Romero-Isart, O. et al. Phys. Rev. Lett. **107**, 020405 (2011).

[16] Li, T., Kheifets, S. & Raizen, M. G. Nature Phys. **7**, 527–530 (2011).

[17] Gieseler, J., Deutsch, B., Quidant, R. & Novotny, L. Phys. Rev. Lett. **109**, 103603 (2012).

[18] Alvarez, C. Undergraduate honors thesis, University of Colorado (2012).

[19] Schlosshauer, M. A. Decoherence and the Quantum-To-Classical Transition (Springer, 2007), 1st edn.

[20] Everett, H. Ph.D. thesis, Princeton University (1956).

[21] Zurek, W. H. Phys. Rev. **26**, 1862–1880 (1982).

[22] Purdy, T. P. et al. Phys. Rev. Lett. **105**, 133602 (2010).

[23] Brahms, N., Botter, T., Schreppler, S., Brooks, D. & Stamper-Kurn, D. Phys. Rev. Lett. **108**, 133601 (2012).

[24] van Wezel, J., Oosterkamp, T. & Zaanena, J. Phil. Mag. **88**, 10051026 (2008).

[25] Werth, G. Trapped Charged Particles and Fundamental Interactions, chap. Principles of Ion Traps. In Blaum & Herfurth [39] (2008).

[26] Ziaeian, I. et al. Int. J. Mass Spec. **304**, 25–28 (2011).

[27] Pearson, C. E. et al. Phys. Rev. A **73**, 032307 (2006).

[28] Li, T. Ph.D. thesis, University of Texas at Austin (2012).

[29] Griffiths, D. Introduction to Electrodynamics (Prentice-Hall, 1999), 3rd edn.

[30] Harada, Y. & Asakura, T. Optics Comm. **124**, 529–541 (1996).

[31] Ashkin, A. & Dziedzic, J. M. App. Phys. Lett. **30**, 202–204 (1977).

[32] Berg-Sorensen, K. & Flyvbjerg, H. Rev. Sci. Instrum. **75**, 3 (2004).

[33] Schlemmer, S., Illemann, J., Wellert, S. & Gerlich, D. J. App. Phys. **90**, 5410 (2001).

[34] McCann, L. I., Dykman, M. & Golding, B. Nature **402**, 6763 (1999).

[35] Li, T., Kheifets, S., Medellin, D. & Raizen, M. G. Science **328**, 5986 (2010).

[36] March, R. E. J. Mass Spec. **32**, 351–369 (1997).

[37] Kildal, A. Contrib. Plasma Phys. **39**, 349–358 (1999).

[38] Unruh, W. & Zurek, W. H. Phys. Rev. D **40**, 1071–1094 (1989).

[39] Blaum, K. & Herfurth, F. (eds.) Trapped Charged Particles and Fundamental Interactions (Springer, 2008).

Appendix A

Density Matrices

In quantum mechanics, there are fundamental limits to the amount of information that can be known simultaneously about certain physical properties. This fact contrasts with classical mechanics, where in principle, it is possible to know all properties of a system to arbitrary precision. However, even when studying a classical system there is often uncertainty in the system's physical properties. This uncertainty usually exists because the system contains so many degrees of freedom that it would be impossible to know the microscopic properties of all parts of the system. When studying system-environment interaction in quantum mechanics, both of these types of uncertainty need to be taken into account. This is possible if the system-environment combination is described by a density matrix. Starting with just the system, the density matrix of a statistical mixture of pure quantum states can be defined as,

$$\rho = \sum_n W_n \mid \psi_n\rangle\langle\psi_n \mid \quad . \tag{A.1}$$

where any $\mid \psi_n\rangle$ can itself represent the superposition of any choice of basis states. Assuming the $\mid \psi_n\rangle$ form an orthonormal basis, the relative proportion of a particular pure state $\mid \psi_m\rangle$ existing in this statistical mixture can be found by taking the expectation value of ρ, $\langle\psi_m \mid \rho \mid \psi_m\rangle = W_m$. As shown in [19], the expectation value of some observable A can be found by taking the trace of ρA,

$$\begin{aligned} tr(\rho A) &= \sum_n \langle\psi_n \mid \rho A \mid \psi_n\rangle = \sum_{n,j} \langle\psi_n \mid \rho \mid \psi_j\rangle\langle\psi_j \mid A \mid \psi_n\rangle \\ &= \sum_{n,i,j} W_i \langle\psi_n \mid \psi_i\rangle\langle\psi_i \mid \psi_j\rangle\langle\psi_j \mid A \mid \psi_n\rangle = \sum_n W_n \langle\psi_n \mid A \mid \psi_n\rangle = \langle A\rangle \end{aligned}$$

Appendix B

Decoherence

In his review of decoherence [1], Zurek gives a rough and general description of the process of decoherence. His general argument is outlined below, using a system described by a basis of $\mid n\rangle$ states. The first step in describing system-environment interaction in quantum mechanics is the introduction of a quantum measuring device. If the states of the system are written as $\mid n\rangle$, then the states of a measuring device can be written as $\mid d_n\rangle$, where the system-device interaction leads to states of the form $\mid \phi^c\rangle = \sum_n a_n \mid n\rangle \mid d_n\rangle$. The result of this interaction appears to contain the information needed to determine the state of the system— if the device is found in the state $\mid d_n\rangle$, then it must be the case that the system is in the state $\mid n\rangle$. The problem is that the device is not in a well-defined state $\mid d_n\rangle$. It is, in fact, in a superposition of states. The density matrix of this post-interaction system-device state is

$$\mid \phi^c\rangle\langle\phi^c \mid = \sum_{n,m} a_n a_m \mid n\rangle \mid d_n\rangle\langle m \mid \langle d_m \mid \quad . \tag{B.1}$$

If this density matrix contained only diagonal terms, then the diagonal coefficients $|a_n|^2$ could be interpreted as the classical probability of the system being in a state $\mid n\rangle$, but this interpretation is not possible when the matrix contains off-diagonal elements. In order to produce a density matrix with only diagonal elements, the measuring device must be coupled to an environment with a large number of degrees of freedom. In that case, the system-device-environment states can be written as $\mid \phi^c\rangle \mid \epsilon\rangle$ (the environments state is given by $\mid \epsilon\rangle$) and the coupling of the device and environment produces states of the form $\sum_n a_n \mid n\rangle \mid d_n\rangle \mid \epsilon_n\rangle$. The system-device density matrix can then be found by tracing over the environment states, $\rho = \sum_i \langle \epsilon_i \mid \phi^c\rangle\langle\phi^c \mid \epsilon_i\rangle = \sum_n a_n a_n^* \mid n\rangle \mid d_n\rangle\langle n \mid \langle d_n \mid$. (4) By tracing over the environment states, the assumption is made that the information contained

in the environments degrees of freedom is not measurable and cannot be recovered by the system. After this environment interaction has taken place, the density matrix describing the system and device is diagonal, so the system is in a classical mixture of pure states of the $\mid n\rangle$ basis. The process described above does not explicitly explain how the off-diagonal elements of the density matrix disappear due to environment interaction. To see how this happens, an explicit example is needed. A common environment used in these kinds of studies is a collection of coupled harmonic oscillators. As shown by Unruh and Zurek [38], the density matrix of a particle in this environment can be described by the equation,

$$\frac{\partial \rho}{\partial t} = -\frac{i}{\hbar}[H, \rho] - \gamma(x - x')\left(\frac{\partial \rho}{\partial x} - \frac{\partial \rho}{\partial x'}\right) - \frac{2m\gamma k_B T}{\hbar^2}(x - x')\rho \tag{B.2}$$

where H is the particle's Hamiltonian and γ is the relaxation rate of the interaction. In a classical system, this last term would describe the Brownian motion of the particle due to interactions with the environment, but in this case it causes the decay of the off-diagonal elements of the particle's density matrix. For example, the density matrix described by a superposition of position states will have $x - x' = 0$ for diagonal elements and $x - x' = \Delta x$ for off-diagonal elements (Δx describes the separation of the superposed states). So these off-diagonal elements will disappear over time while the diagonal elements will not. The result is a classical mixture of localized wavepackets. [38]

In the end, the process of decoherence gives the same result as a measurement in the Copenhagen interpretation, but it accomplishes this outcome using only the unitary time evolution of states as described by the Schrodinger equation (von Neumann version for density matrices).

Appendix C

Measurement calibration

The signal from the quadrant photodetector can be calibrated to find the particle's displacement in μm. Using this calibration factor β, the power spectrum can be given in terms of $S(\mu m^2 Hz^{-1})$ and the temperature can be calculated absolutely without having to compare multiple power spectrums. This calibration factor requires knowledge of two relationships— the positioning electrode voltage versus particle displacement and the positioning electrode voltage versus signal voltage. For displacements much smaller than the radius of particle, there is a linear relationship between the positioning electrode voltage and the signal voltage. Likewise, for displacements much smaller than the electrode separation, the microsphere position is linear with the feedback voltage. Figure C.1 shows calibration data in the ion trap for the relationship between input and signal voltages. Combining both the calibration factors gives $\beta = 1.32 \pm 0.15\ \mu m/V$.

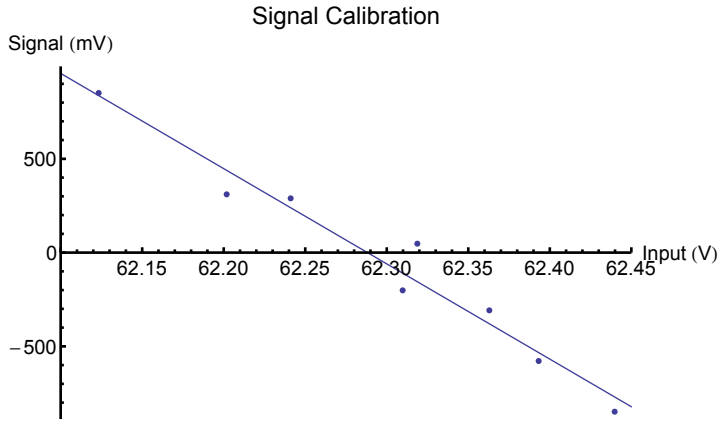

Figure C.1: Input voltages to y-axis positioning electrodes and the respective output signals from the quadrant photodetector.

Appendix D

Measurement error and feedback

The measurement error in this experiment can be broken into two categories. First, there is the electronic noise added by the photodetectors and all of the feedback circuitry. The temperature dependence of this noise is analyzed in [4], it is found that the closed-loop temperature in the presence of measurement noise is given by

$$T = \frac{T}{1+g} + \frac{\Gamma_0 \omega_0^2}{4k_B}\left(\frac{g^2}{1+g}\right) \tag{D.1}$$

for noise spectrum S_n and derivative gain $g = \Gamma_{fb}/\Gamma_0$. The second source of measurement error is related to the existence of three different coordinate systems in this experiment. These are the system formed by the trap axes, that formed by the measurement axes, and that formed by the feedback axes. If these axes are rotated relative to one another, the feedback system will produce coupling between the motion along different trap axes. This coupling set the temperature limit in the experiments by Li, Kheifets, and Raizen [16]. In the supplementary information to [16] an expression for the power spectrum is derived in terms of a linear combination of the signals for all three measurement axes. This expression describes the result of misalignment between the measurement and trap axes. In our experiment these axes are very close to parallel, and the main source of coupling is the misalignment between the trap and feedback axes. In this experiment, the ring-shaped electrodes which control feedback along the x-axis (see Fig. 5.2) are the main source of this misalignment. Figure D.1 demonstrates this coupling. A different geometry of feedback electrodes may help to minimize coupling along different axes.

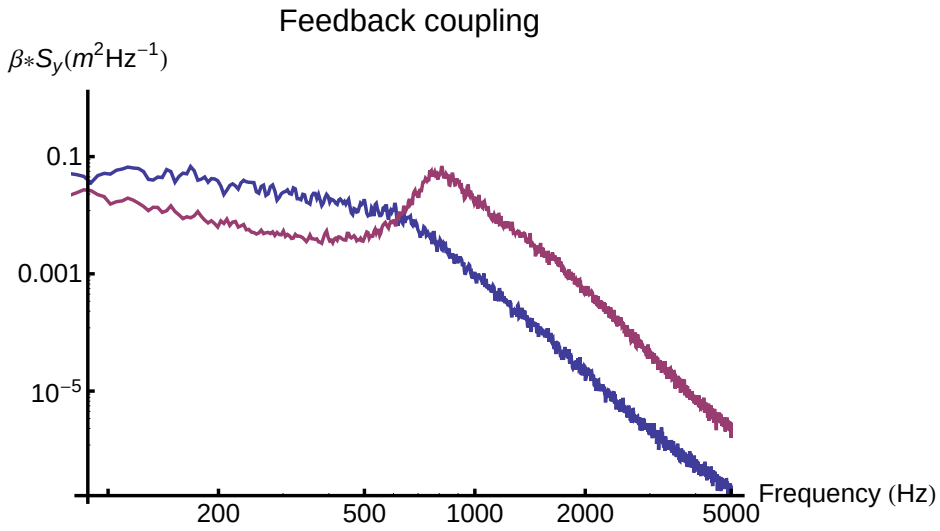

Figure D.1: Power spectrums for y-axis with no feedback (purple) and with derivative feedback along the x-axis (blue).